

# Posterior-Aided Regularization for Likelihood-Free Inference

Dongjun Kim<sup>1</sup> Kyungwoo Song<sup>1</sup> Seungjae Shin<sup>1</sup> Wanmo Kang<sup>1</sup> Il-Chul Moon<sup>1</sup>

## Abstract

The recent development of *likelihood-free inference* aims training a flexible density estimator for the target posterior with a set of input-output pairs from *simulation*. Given the diversity of simulation structures, it is difficult to find a single unified inference method for each simulation model. This paper proposes a universally applicable regularization technique, called Posterior-Aided Regularization (PAR), which is applicable to learning the density estimator, regardless of the model structure. Particularly, PAR solves the mode collapse problem that arises as the output dimension of the simulation increases. PAR resolves this posterior mode degeneracy through a mixture of 1) the reverse KL divergence with the mode seeking property; and 2) the mutual information for the high quality representation on likelihood. Because of the estimation intractability of PAR, we provide a unified estimation method of PAR to estimate both reverse KL term and mutual information term with a single neural network. Afterwards, we theoretically prove the asymptotic convergence of the regularized optimal solution to the unregularized optimal solution as the regularization magnitude converges to zero. Additionally, we empirically show that past sequential neural likelihood inferences in conjunction with PAR present the statistically significant gains on diverse simulation tasks.

## 1. Introduction

The development of computing power has motivated building simulation models, which are complex in order to become high-fidelity. A complex simulation model is constructed as a generative process, so the likelihood function is modeled in an implicit way. This implicit nature of the likelihood yields the inference task challenging, and we call

<sup>1</sup>KAIST, Republic of Korea. Correspondence to: Il-Chul Moon <icmoon@kaist.ac.kr>.

Preliminary work. Under review by the International Conference on Machine Learning (ICML).

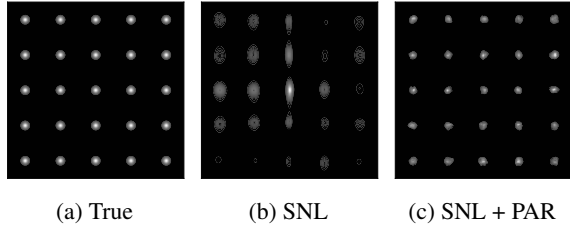


Figure 1. Comparison of (a) true posterior (see Appendix A) to approximate posteriors with (b) SNL and (c) the regularized SNL. SNL with PAR performs better than the vanilla SNL within limited simulation budget in 1) capturing multiple modes and 2) acquiring roundy shape of each mode.

the inference on the implicit likelihood as *likelihood-free inference*. Recent algorithms on *likelihood-free inference* introduced the amortized learning of a posterior distribution with a set of input-output pairs from the simulation model.

The recent algorithms iteratively improve the approximation on the posterior to the exact posterior by rounds. This approximation hinges upon the budget of executing the simulation models, and the approximated posterior would be immature if the budget is limited. In particular, if the model attains a multi-modal posterior distribution<sup>1</sup>, Figure 1 shows the failure of posterior inference with a previous algorithm, Sequential Neural Likelihood (SNL) (Papamakarios et al., 2019). Also, we observe that the inference gets worse by capturing fewer modes in the posterior as the dimensionality of the model outcome increases.

While this mode collapse is largely resolved as the number of training data increases, it is difficult to gather the sufficient size of a dataset for training on simulations because of long execution time. This specific phenomenon in the *likelihood-free inference* motivates a widely applicable research question in the machine learning community: recovering a complex distribution with limited training instances. If we focus on the data limitation, we may choose methods to avoid overfitting. However, such avoidance will also limit

<sup>1</sup>When the generative model architecture is fixed throughout the inference, the posterior distribution needs to be complex to reflect the real world, compared to either simple uniform or Normal distributions as a source of stochasticity. Such model architecture includes the internal coefficients, the agent mechanisms, the equation dynamics, etc.

the complexity of the model distribution; so, for instance, the multi-modality would not be captured fully. Moreover, the model distribution complexity should increase as the distribution lies on a high dimensional space<sup>2</sup>, and as the distribution has fine details on its domain space.

Given this trade-off between the overfitting avoidance and the modeled posterior complexity, this paper proposes a regularization method that avoids overfitting by minimally affecting the posterior distribution complexity. Specifically, the regularization is designed to capture the multi-modal and the high dimensional aspects of the posterior distribution. We name this regularization as Posterior-Aided Regularization (PAR), which significantly outperforms the baseline algorithms in every experimental case.

PAR introduces the reverse KL regularization that attains the *mode seeking* property to enhance the dataset efficiency, when the training dataset is constructed in a cumulative way for every round by executing additional simulations. Also, PAR proposes the mutual information regularization between the simulation input and the output in order to capture rich representations that ultimately find the complex posterior with a limited budget. In addition, we estimate the mixed regularization in a unified way with a single network structure, and we analyze PAR theoretically by providing the *unique* closed-form solution of the regularized loss.

## 2. Previous Research

### 2.1. Problem Definition

The evaluation on conditional likelihood of  $p(x|\theta)$  in *simulation* is not allowed because *simulation* is fundamentally a data-generation process from its input  $\theta$  to an output  $x$ . The purpose of *likelihood-free inference* is the estimation of the posterior distribution of  $p(\theta|x=x_o)$  where  $x_o$  is a single shot of a real-world observation<sup>3</sup>.

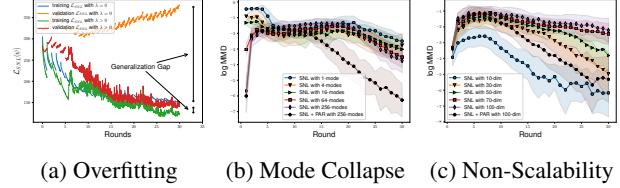
### 2.2. Sequential Likelihood-Free Inference

Recent approaches of *likelihood-free inference* estimate the posterior with the multiple rounds of inference steps. This iterative inference gradually fastens the approximate posterior to the exact posterior by optimizing the neural network parameters used for inference. This *sequential neural* approach is becoming the mainstream in the community of likelihood-free inference because the iterative amortized optimization saves simulation budget by orders of magnitude.

At the initial round, the sequential likelihood-free inference gathers simulation inputs from the prior distribution,  $p(\theta)$ .

<sup>2</sup>This may happen if a raw simulation outcome is not filtered by a set of summary statistics.

<sup>3</sup>Assuming that the real-world with the same context happens only *once*.



(a) Overfitting (b) Mode Collapse (c) Non-Scalability

Figure 2. SNL with no regularization ( $\lambda = 0$ ) on SLCP-16 simulation (see Appendix A) suffers from (a) large generalization gap (b) inaccurate posterior estimation on multi-modal posterior (c) slow learning on high dimensional output.

A collection of simulation input-output pairs constructs a dataset for the initial round,  $\mathcal{D}_1 = \{(\theta_{1,j}, x_{1,j})\}_{j=1}^N$ , where each  $x_{1,j}$  is the simulation output corresponds to  $\theta_{1,j}$ , i.e.  $x_{1,j} \sim p(x|\theta_{1,j})$ . If we were to infer the joint distribution at the first round, the inference objective becomes the maximization of the likelihood, or equivalently the minimization of its corresponding KL loss,  $q_1(\theta, x) = \arg \min_q \mathcal{L}(q; \mathcal{D}_1)$ . For the next rounds, the new batch of simulation inputs are drawn from a proposal distribution, i.e.  $\theta_{r,j} \sim p_r(\theta) \propto p(\theta)q_{r-1}(x_o|\theta)$  for  $j = 1, \dots, N$ , and the next batch is cumulated to the existing dataset as  $\mathcal{D}_r \leftarrow \mathcal{D}_{r-1} \cup \{(\theta_{r,j}, x_{r,j})\}_{j=1}^N$ , and the inference repeats the minimization of the loss function, again. This iterative inference on the joint distribution eventually estimates the desired posterior distribution.

Sequential Neural Likelihood proposes a neural likelihood to model the joint distribution,  $\tilde{q}_\psi(\theta, x) = \tilde{p}(\theta)q_\psi(x|\theta)$ , parametrized by  $\psi$ . Here, the cumulative dataset is collected from different input distributions at each round, so we denote  $\tilde{p}(\theta)$  to be the expected proposal distributions,  $\tilde{p}(\theta) = \frac{1}{r} \sum_{s=1}^r p_s(\theta)$ , over rounds. SNL loss is  $\mathcal{L}_{SNL}(\psi) = -\mathbb{E}_{\tilde{p}(\theta)p(x|\theta)} [\log q_\psi(x|\theta)] = D_{KL}(\tilde{p}(\theta, x), \tilde{q}_\psi(\theta, x)) + \text{const}$ , where  $\tilde{p}(\theta, x)$  is the true distribution decomposed by  $\tilde{p}(\theta)p(x|\theta)$ , and  $\tilde{q}_\psi(\theta, x)$  is the model distribution decomposed by  $\tilde{p}(\theta)q_\psi(x|\theta)$ . Therefore, the optimal neural likelihood,  $q_{\psi^*}(x|\theta)$ , matches to the exact likelihood,  $p(x|\theta)$ , in the support of  $\tilde{p}(\theta)$  when the KL divergence vanishes.

### 2.3. Multimodal and High Dimensional Outputs

In spite of the flexibility on the posterior inference by SNL, it suffers from the overfitting as in Figure 2 (a) with a large generalization gap. In consequence, Figure 2 presents that SNL hardly infers the posterior when (b) the posterior distribution attains multiple modes, and (c) the simulation output is high dimensional. Assuming that the posterior inference on SNL is sub-optimal, the additional data from this inaccurate posterior would lower the data quality, and the poorly constructed data would reinforce the sub-optimality of SNL. This natural feedback loop of inference inaccuracy and inefficient training data collection limits the further utilization of SNL in the *likelihood-free inference* community.

### 3. Design of Posterior-Aided Regularization

As the previous section asserts the scalability with respect to the output dimension and the modes, the current version of SNL needs to be constrained by a regularization to prevent the negative feedback of fitting the inaccurate posterior distribution. We introduce a constrained problem as an alternative of SNL as the below.

$$\begin{aligned} & \text{minimize } \mathcal{L}_{SNL}(\psi) \\ & \text{subject to } F(\psi) \leq C. \end{aligned} \quad (1)$$

The constraint restricts the class of distributions to be among  $\mathcal{F} = \{q_\psi : F(\psi) \leq C\}$ , so our objective becomes the design of  $\mathcal{F}$ . The constrained problem of Eq. 1 is equivalent to the minimization of an unconstrained Lagrangian function:

$$\mathcal{L}^\lambda(\psi) = \mathcal{L}_{SNL}(\psi) + \lambda F(\psi),$$

where  $\lambda > 0$  is the regularization magnitude.

To determine a specific form of the constraint, we analyze the slow learning of SNL in terms of its loss design. SNL optimizes the forward KL divergence between the true joint distribution,  $\tilde{p}(\theta, x) = \tilde{p}(\theta)p(x|\theta)$ , and the model joint distribution,  $\tilde{q}_\psi(\theta, x) = \tilde{p}(\theta)q_\psi(x|\theta)$ . The forward KL divergence is well-known for its *mode-covering* property (Ke et al., 2019; Zhang et al., 2019), so SNL prefers a widespread distribution over a localized distribution to lower the forward KL divergence.

SNL forgets searching divisive modes at the intermediate rounds because the *mode-covering* property enforces gathering data instances from a widespread posterior, rather than a clustered posterior distribution. Eventually, the collected data becomes spread across the whole domain of  $\theta$ , and those  $\theta$  samples, which are out of modes, do not contribute to the inference performance significantly. In addition, such instances hinder the learning due to the negative reinforce mechanism in Section 2.3.

As we observed the source of inefficiency within SNL, we discovered that SNL would be better off by adding a constraint for the exploitation rather than the exploration because of the *mode covering* by the forward KL. Therefore, we introduce a regularization as below to provide the force of exploitation, as well as the force of enhancing representation power to reduce the required simulation budget.

$$F(\psi) = F^{(1)}(\psi) + F^{(2)}(\psi),$$

with  $F^{(1)}(\psi) = D_{KL}(\tilde{q}_\psi(\theta, x), \tilde{p}(\theta, x))$ , and  $F^{(2)}(\psi) = -\mathbb{I}(\Theta, X)$ , where we denote random variables using upper-case letters (e.g.  $\Theta, X$ ), and their realizations by the corresponding lower-case letters (e.g.  $\theta, x$ ).

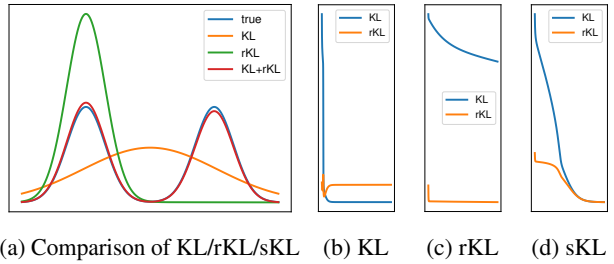


Figure 3. (a) Comparison of distributions estimated by KL, reverse KL, and symmetric KL (KL + rKL) to the true distribution. (b,c,d) The estimated KL and reverse KL values when the loss function to optimize is (b) KL, (c) reverse KL, and (d) symmetric KL.

#### 3.1. $F^{(1)}$ : Regularization for Mode Seeking

The first term of  $F^{(1)}$  is the reverse KL divergence between  $\tilde{p}(\theta, x)$  and  $\tilde{q}_\psi(\theta, x)$ . As a counterpart of the forward KL, the reverse KL has the *mode-seeking* property (Nguyen et al., 2017; Poole et al., 2016), so the reverse KL prefers mode-concentrated distributions. This property stems from penalizing distributions with non-zero values wherever  $\tilde{q}_\psi > \tilde{p}$  because the reverse KL integrand,  $\log \frac{\tilde{q}_\psi}{\tilde{p}}$ , becomes large on a region of  $\tilde{q}_\psi > \tilde{p}$ . In other words, the reverse KL strongly penalizes a mode-covering distribution with non-zero values on the intermediate region between modes, whereas such distribution is preferred by SNL.

Moreover, the forward KL divergence is neither weaker nor stronger than the reverse KL divergence, which means that there is no inequality relation between the two of them. Because of this incomparability, the forward and the reverse KL divergences induce distinctive topologies on the space of probability distributions. Therefore, the SNL constrained with the reverse KL is not reducible to the unregularized SNL, and the suggested constrained problem generates a different optimization path.

The weighted divergence,  $\mathcal{L}_{SNL}(\psi) + \lambda F^{(1)}(\psi)$ , mixes two extremes in a unified optimization loss by taking both contrastive properties inherited by forward and reverse KLS. The minimization of the weighted divergence searches distributions with accurate modes by the *mode-seeking* property while retaining the mode variability by the *mode-covering* property. The weight of  $\lambda$  controls the exploration-exploitation effect by influencing the sample diversity and the sample quality for the next round. Given this posterior update, the cumulative dataset includes the samples of  $\theta$ , which are clustered around modes (Zhang et al., 2019) if  $\lambda$  becomes high. On the contrary, the cumulative dataset would spread out if  $\lambda$  becomes low.

Figure 3 empirically demonstrates the arguments discussed above: (a) the weighted divergence captures two-modals, whereas neither KL nor reverse KL infers the groundtruth distribution; (b,c,d) the weighted divergence minimizes both

KL/reverse KL divergences, whereas neither of two extremes optimizes the corresponding opposite extreme divergence.

### 3.2. $F^{(2)}$ : Regularization for Representation Quality

Another regularization component,  $F^{(2)}$ , utilizes the mutual information to mitigate the slow learning of SNL. Although the mutual information solves the mode collapse in many applications (Lee et al., 2020; Peng et al., 2020), we emphasize the mutual information for its scalability of representation learning on high dimensions (Hjelm et al., 2018; Bachman et al., 2019; Zhao et al., 2017). The mutual information measures the amount of information obtained from  $X$  by observing  $\Theta$ , which is defined by  $\mathbb{I}(\Theta, X) = \mathbb{H}(X) - \mathbb{H}(X|\Theta)$ , where  $\mathbb{H}(X|\Theta)$  is the conditional entropy,  $\mathbb{H}(X|\Theta) = -\int \tilde{p}(\theta) \int q_\psi(x|\theta) \log q_\psi(x|\theta) dx d\theta$ .

SNL regularized with the mutual information provides a highly predictable model to discriminate  $\theta$  given  $x$ . First, we discuss the localization effect of  $\mathbb{H}(X|\Theta = \theta)$ . To maximize  $\mathbb{I}$ ,  $\mathbb{H}(X|\Theta = \theta)$  should be minimized, which means the lower conditional entropy is preferred. Therefore,  $q_\psi(x|\theta)$  will be localized in the  $x$ -space. Second, we focus on the discriminative effect of  $H(X)$ . The maximization of  $\mathbb{I}$  increases  $H(X)$ , so the higher entropy is preferred. To increase the entropy,  $\tilde{q}_\psi(x) = \int \tilde{p}(\theta) q_\psi(x|\theta) d\theta$  should be flattened, so this entropy will enforce  $q_\psi(x|\theta) \neq q_\psi(x|\theta')$ .

Figure 4 illustrates the effect of mutual information on inference. If we define the mutual information ratio as  $r_\psi = \frac{D_{KL}(q_\psi(\theta, x), \tilde{p}(\theta) \tilde{q}_\psi(x))}{D_{KL}(\tilde{p}(\theta, x), \tilde{p}(\theta) \tilde{p}(x))}$ , then  $r_\psi = 1$  if and only if  $q_\psi(x|\theta) = p(x|\theta)$ . The ratio of the unregularized SNL saturates at the sub-optimal in Figure 4, so the additional term of maximizing the mutual information enforces to reach the learning curve to  $r_\psi = 1$ . Figure 4 empirically demonstrates that SNL regularized with the mutual information estimates the exact likelihood by the neural network after rounds of inference.

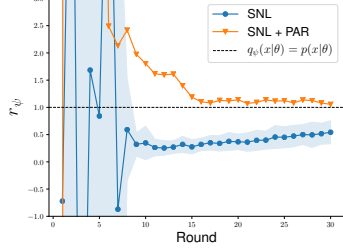


Figure 4. Comparison of ratios  $r_\psi$  with/without mutual information regularization on SLCP-16 simulation (see Appendix A).

## 4. Estimation of Posterior-Aided Regularization

### 4.1. Unified Estimation of Reverse KL and Mutual Information

While the constraint of  $F$  provides a useful implication by avoiding the inefficient feedback loop between intermediate

inference inaccuracy and poorly cumulated dataset, the proposed constraint cannot be tractably calculated. Therefore, additional optimization is indispensable for the estimation of  $F(\psi)$ . Although there are estimation methods for the reverse KL and the mutual information individually, a simultaneous estimation of both terms has not been introduced yet. This paper proposes a method to estimate both  $F^{(1)}$  and  $F^{(2)}$  with a single neural network.

In contrast to the previous estimation methods, we use neither variational inference (Poole et al., 2019) nor minimax framework (Belghazi et al., 2018; Nowozin et al., 2016). Instead, we estimate the constraint by approximating the joint distribution with posterior modeling, so we name this estimator as Posterior-Aided Regularization (PAR). PAR updates the approximation of the joint distribution at each round by training the posterior model in the alternative order with SNL, as suggested in Algorithm 1.

### 4.2. Proxy of Regularization

If we define a surrogate constraint to be

$$\hat{F}(\psi) = -\mathbb{E}_{\tilde{p}(\theta)q_\psi(x|\theta)} [\log \tilde{p}(\theta|x)], \quad (2)$$

where  $\tilde{p}(\theta|x) = \tilde{p}(\theta) \frac{p(\theta|x)}{\tilde{p}(\theta)} \frac{p(x)}{\tilde{p}(x)}$  with  $\tilde{p}(x) = \int \tilde{p}(\theta, x) d\theta$ , then Theorem 3 inspects the relation of  $F$  and  $\hat{F}$  by providing the decomposition of  $\hat{F}$ . See Appendix B for proof.

**Theorem 1.** Suppose  $\hat{F}(\psi)$  is defined to be  $-\mathbb{E}_{\tilde{p}(\theta)q_\psi(x|\theta)} [\log \tilde{p}(\theta|x)]$ , then  $\hat{F}(\psi)$  is decomposed into  $\hat{F}(\psi) = \hat{F}^{(1)}(\psi) + F^{(2)}(\psi) + \text{const.}$  with

$$\hat{F}^{(1)}(\psi) = D_{KL}(\tilde{q}_\psi(x) \tilde{q}_\psi(\theta|x), \tilde{q}_\psi(x) \tilde{p}(\theta|x))$$

$$F^{(2)}(\psi) = -\mathbb{I}(\Theta, X).$$

The second decomposition of  $\hat{F}(\psi)$  is the mutual information, so the surrogate constraint yields the exact estimation of the mutual information. On the other hand, the first decomposition of  $\hat{F}^{(1)}(\psi)$  is a perturbation of the exact reverse KL divergence,  $F^{(1)}(\psi) = D_{KL}(\tilde{q}_\psi(x) \tilde{q}_\psi(\theta|x), \tilde{p}(x) \tilde{p}(\theta|x))$ , and we name  $\hat{F}^{(1)}(\psi)$  as a *modified* reverse KL divergence. This modified reverse KL divergence becomes the exact reverse KL divergence if the neural likelihood is the exact likelihood:

$$\hat{F}^{(1)}(\psi^*) = F^{(1)}(\psi^*) \quad \text{with} \quad \psi^* = \arg \min_{\psi} \mathcal{L}_{SNL}(\psi).$$

Therefore, the surrogate constraint,  $\hat{F}(\psi)$ , is a proxy of the original constraint,  $F(\psi)$ .

### 4.3. Estimation Method

Posterior-Aided Regularization (PAR) estimates the proxy of the regularization in Eq. 2 from the estimation of the

**Algorithm 1** Posterior-Aided Likelihood

---

```

for  $r = 1$  to  $R$  do
    if  $r = 1$  then
        Draw simulation inputs  $\{\theta_{1,j}\}_{j=1}^N$  from prior  $p(\theta)$ 
    end if
    if  $r > 1$  then
        Draw simulation inputs  $\{\theta_{r,j}\}_{j=1}^N$  from proposal
         $p_r(\theta) \propto q_{r-1}(x_o|\theta)p(\theta)$ 
    end if
    for  $j = 1$  to  $N$  do
        Simulate  $x_{r,j} \sim p(x|\theta_{r,j})$ 
    end for
    Add  $(\theta_{r,j}, x_{r,j})$  into the training data  $\mathcal{D}_r \leftarrow \mathcal{D}_{r-1} \cup$ 
     $\{(\theta_{r,j}, x_{r,j})\}_{j=1}^N$  (assuming  $\mathcal{D}_0 = \emptyset$ )
    repeat
        Update  $\phi \leftarrow \phi - \nabla_\phi \mathcal{L}_{APT}(\phi; \mathcal{D}_r)$ 
        Update  $\psi \leftarrow \psi - \nabla_\psi \mathcal{L}_\phi^\lambda(\psi; \mathcal{D}_r)$ 
    until converged
end for

```

---

posterior distribution,  $\tilde{p}(\theta|x)$ , through Automatic Posterior Transformation (APT) (Greenberg et al., 2019). APT estimates the posterior distribution with a loss

$$\mathcal{L}_{APT}(\phi) = -\mathbb{E}_{\tilde{p}(\theta)p(x|\theta)} [\tilde{q}_\phi(\theta|x)],$$

where  $\tilde{q}_\phi(\theta|x) = \tilde{p}(\theta) \frac{q_\phi(\theta|x)}{p(\theta)} \frac{1}{Z(x;\phi)}$  with  $Z(x;\phi)$  to be a normalization function. Here, APT models the posterior distribution,  $q_\phi(\theta|x)$ , with a normalizing flow, parametrized by  $\phi$ . APT loss is equivalent to the KL divergence,  $\mathcal{L}_{APT}(\tilde{p}(\theta)p(x|\theta), \tilde{p}(x)\tilde{q}_\phi(\theta|x))$ , and the optimal solution of this KL divergence satisfies  $\tilde{q}_{\phi^*}(\theta|x) = \tilde{p}(\theta|x)$ .

We estimate Eq. 2 by

$$\hat{F}_\phi(\psi) = -\mathbb{E}_{\tilde{p}(\theta)q_\psi(x|\theta)} [\log \tilde{q}_\phi(\theta|x)]. \quad (3)$$

The estimation on PAR becomes exact if the posterior estimation of APT becomes exact:

$$\hat{F}_{\phi^*}(\psi) = \hat{F}(\psi) \quad \text{with} \quad \phi^* = \arg \min_\phi \mathcal{L}_{APT}(\phi).$$

Analogous to Theorem 3, Eq. 3 is decomposed by

$$\hat{F}_\phi(\psi) = \hat{F}_\phi^{(1)}(\psi) + F^{(2)}(\psi) + \text{const.},$$

with  $\hat{F}_\phi^{(1)}(\psi) = D_{KL}(\tilde{q}_\psi(x)\tilde{q}_\psi(\theta|x), \tilde{q}_\psi(x)\tilde{q}_\phi(\theta|x))$ .

The time complexity of our model is bounded by the linear summation of the complexity on SNL and APT, see Appendix C for the complexity analysis in big-O notations.

## 4.4. Theoretic Analysis

### 4.4.1. MODIFIED REVERSE KL DIVERGENCE

As the reverse KL divergence is perturbed as a *modified* reverse KL divergence, this section investigates the effect

of the perturbation on the optimality. We conclude that the perturbation does not arise the ill-posedness by showing the uniqueness of  $\arg \min_{q_\psi} \mathcal{L}_{SNL}(\psi) + \lambda \hat{F}^{(1)}(\psi)$ .

The optimal solution of the modified reverse KL divergence,  $\hat{F}^{(1)}(\psi) = D_{KL}(\tilde{q}_\psi(x)\tilde{q}_\psi(\theta|x), \tilde{q}_\psi(x)\tilde{p}(\theta|x))$ , satisfies  $\tilde{q}_{\psi^*}(\theta|x) = \tilde{p}(\theta|x)$ . Having that  $\tilde{p}(\theta|x) = \tilde{p}(\theta) \frac{p(\theta|x)}{p(\theta)} \frac{p(x)}{\tilde{p}(x)}$ ,  $q$  is the solution of  $\arg \min_{q_\psi} \hat{F}^{(1)}(\psi)$  if and only if

$$\frac{p(x|\theta)}{\tilde{p}(x)} = \frac{q(x|\theta)}{\tilde{q}(x)}. \quad (4)$$

While the solution of  $q$  could be more than one instance, this potential ill-posedness does not prevent the uniqueness when we include  $\mathcal{L}_{SNL}(\psi)$ , as well. The exact likelihood,  $\tilde{p}(\theta|x)$ , satisfies Eq. 4, so the exact likelihood belongs to the solution of  $\arg \min_{q_\psi} \hat{F}^{(1)}(\psi)$ . Thus, the exact likelihood minimizes both SNL loss and modified reverse KL loss. Particularly, the exact likelihood *uniquely* minimizes the SNL loss, and this uniqueness on SNL loss guarantees the uniqueness of the minimization problem for the weighted loss,  $\arg \min_{q_\psi} \mathcal{L}_{SNL}(\psi) + \lambda \hat{F}^{(1)}(\psi)$ . Therefore, we conclude that the perturbation does not arise ill-posedness if the modified reverse KL is combined with the SNL loss.

### 4.4.2. ASYMPTOTIC CONVERGENCE

In addition to the optimality analysis of the perturbation with respect to the first term, maximizing the mutual information,  $F^{(2)}(\psi)$ , inhibits the neural likelihood from estimating the exact likelihood when  $\lambda > 0$ . To investigate the effect from the mutual information on the optimality, Theorem 4 analyzes the closed-form solution of  $\mathcal{L}_\phi^\lambda(\psi) = \mathcal{L}_{SNL}(\psi) + \lambda \hat{F}(\psi)$ . See Appendix B for the proof.

**Theorem 2.** *Suppose  $p(\theta, x)$  and  $p(\theta)$  are bounded on a positive interval,  $\tilde{p}(\theta)$  is bounded below, and  $q_\psi(\theta, x)$  is uniformly upper bounded on  $\psi$ . Then the optimization problem  $\arg \min_{q_\psi} \mathcal{L}_\phi^\lambda(\psi)$  attains the unique solution of*

$$q_{\psi^*}^\lambda(x|\theta) = \frac{p(x|\theta)}{c(\theta) - \lambda \log \tilde{q}_\phi(\theta|x)},$$

where  $c(\theta)$  is a constant with respect to  $x$  that makes  $q_{\psi^*}^\lambda(x|\theta)$  a distribution in  $x$ -space.

Theorem 4 guarantees that the optimal neural likelihood of the regularized loss,  $\mathcal{L}_\phi^\lambda(\psi)$ , converges to the exact likelihood as the regularizing magnitude converges to zero:  $q_{\psi^*}^\lambda(x|\theta) \rightarrow p(x|\theta)$  as  $\lambda \rightarrow 0$ . As an additional note, this convergence of  $q_{\psi^*}^\lambda(x|\theta)$  is irrelevant to the convergence of the neural posterior,  $\tilde{q}_\phi(\theta|x)$ .

Figure 5 shows the trajectories of the regularized solutions with various  $\lambda$ . Figure 5 visualizes two extremes: 1)  $\lambda = 0$

(blue) represents the vanilla SNL without the regularization, which shows the slow convergence to the global optimum; and 2)  $\lambda = \infty$  (green) counts only the regularization loss without the SNL loss, which deviates largely to the global optimum. The trajectory of non-vanishing  $\lambda = 1$  (orange) shows the empirical evidence of Theorem 4 by slightly deviating from the global optimum. On the other hand, the trajectory with vanishing magnitude (purple) shows the convergence to the global optimum as  $\lambda \rightarrow 0$ . Moreover, the convergence with vanishing  $\lambda$  is faster than the learning curve of SNL.

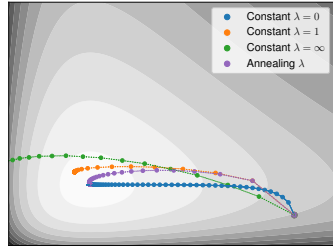


Figure 5. Comparison of training trajectories in a toy example (see Appendix A) with various  $\lambda$ .

## 5. Experiments

We compare our regularization with the baselines as SMC-ABC (Sisson et al., 2007), SNPE-A (Papamakarios & Murray, 2016), SNPE-B (Lueckmann et al., 2018), APT, AALR (Hermans et al., 2020), and SNL on various simulations. First, we test the regularized SNL on tractable simulations with multi-modal posterior distributions. SLCP-16 and SLCP-256 (Kim et al., 2020b) attain tractable likelihoods that allow analyzing the effect of PAR with respect to the Maximum Mean Discrepancy (MMD) (Sriperumbudur et al., 2010) and the Inception Score (IS) (Salimans et al., 2016). MMD measures the inference quality of the posterior, and IS measures the sample diversity for each inference round.

Next, we experiment on realistic simulations without the tractable likelihood formula. The simulations are as follows: 1) the M/G/1 model (Papamakarios et al., 2019) from the queuing theory is a discrete-event simulation that the simulation states update according to discrete events randomly drawn from an exponential distribution with unknown parameters; 2) the Ricker model (Gutmann & Corander, 2016) from the field of ecology is a system dynamics simulation that predicts the latent animal population with observed populations randomly selected from a Poisson distribution with unknown parameters; and 3) the Poisson model (Kim et al., 2020a) in the field of physics is a second-order elliptic partial differential equation that calculates the heat transfers with unknown local diffusivities. See Appendix A for the details on simulations.

### 5.1. Tractable Simulations

#### 5.1.1. SLCP-16

The Simple-Likelihood-and-Complex-Posterior-16 (SLCP-16) (Kim et al., 2020b) is a simulation with 16 modes in

its posterior distribution. Figure 6 presents the marginal posterior distribution inferred by various algorithms, including the proposed method. Compared to the groundtruth posterior in Figure 6 (a), APT in Figure 6 (b) infers an inaccurate posterior with many *wrong* modes. AALR in Figure 6 (c) infers a posterior with unclear separations between modes. The target distribution of AALR is the likelihood-to-evidence ratio,  $\frac{p(x|\theta)}{\bar{p}(x)}$ , which shifts at every round. We hypothesize the unclear separation of AALR due to the overfitting that frequently arises if the target distribution shifts (Shao et al., 2019). The proposed SNL with PAR in Figure 6 (e) captures every mode with clear separations between modes, in contrast to the heavy-tailed inaccurate posterior of SNL in Figure 6 (f) that misses many modes.

Figure 10 presents the experimental result of SLCP-16. Figure 10 (a) demonstrates that SNL with PAR outperforms the baseline algorithms with significant margins. This performance gain is particularly remarkable because the vanilla SNL performs the worst out of the baselines, which indicates that PAR significantly improved SNL. Figure 10 (b) compares the unregularized SNL with the regularized SNL when the output dimension increases. SNL shows the slow performance on every cases of dimension settings while the regularized SNL captures the most of modes on every cases, including on the case of 150-dimensional output.

Table 1 presents the various performances of SLCP-16. The regularized SNL beats the baselines on SLCP-16 for every metric. The best performance of the proposed method induces three implications. First, the best score on the negative log probability at the groundtruth inputs<sup>4</sup>,  $-\log p(\theta^*|x_o)$ , indicates that the inferred posterior is concentrated to the modes, as in Figure 6 (e). Second, the best MMD performance guarantees the best quality of the posterior inference. Third, the best IS indicates the most divisive modalities of the inferred posterior.

#### 5.1.2. SLCP-256

For the study on extremely many modalities, the Simple-Likelihood-and-Complex-Posterior-256 (SLCP-256) (Kim et al., 2020b) is a simulation with 256 modes in its posterior distribution. Figure 11 (a) presents that AALR shows the comparable performance to SNL with PAR after rounds. However, the convergence is slower than the SNL with PAR because SNL with PAR reaches 200 inception score at the 27-th round whereas AALR comes to the similar score at the 40-th round. The vanilla SNL captures various modes in SLCP-256 within an acceptable rounds, but SNL covers

<sup>4</sup>Though we test the simulations with a single *true* input ( $\theta_1^*$ ), there are *alternative* simulation inputs ( $\theta_2^*$ ) that create the same likelihood function,  $p(x|\theta_1^*) = p(x|\theta_2^*)$ . We denote such set of inputs,  $\theta_{1:K}^*$ , as the groundtruth inputs, and we calculate  $-\log p(\theta^*|x_o) := -\sum_{k=1}^K \log p(\theta_k^*|x_o)$ .

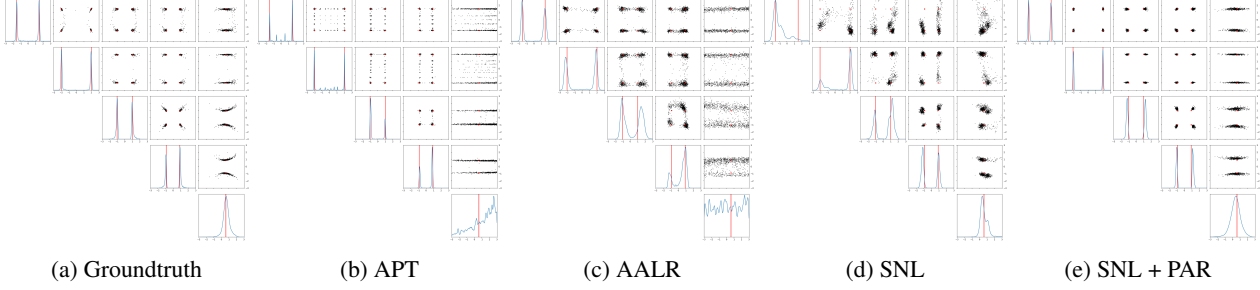


Figure 6. Comparison of marginal posterior distributions on SLCP-16 with 100-dimensional output between (a) groundtruth and (b) APT, (c) AALR, (d) SNL, and (e) SNL regularized by PAR after 40 rounds of inference with 100 simulation budget for each round. Black dots are the samples from approximate posteriors, the red dots are groundtruth simulation inputs, and we plot marginal distribution of each dimension through Kernel Density Estimation.

Table 1. Comparison of performance on (Left) SLCP-16 with 100-dimensional output and (Right) SLCP-256 with 80-dimensional output. On SLCP-16, we run 30 rounds of inference with 100 simulation budget for each round. On SLCP-256, we run 50 rounds of inference with 100 simulation budget for each round. The negative log probability at the groundtruth inputs is scaled by  $10^{-2}$ .

| ALGORITHM    | SLCP-16                           |                                    |                                    | SLCP-256                           |                                    |                                     |
|--------------|-----------------------------------|------------------------------------|------------------------------------|------------------------------------|------------------------------------|-------------------------------------|
|              | $-\log p(\theta^* x_o)$ (↓)       | log MMD (↓)                        | IS (↑)                             | $-\log p(\theta^* x_o)$ (↓)        | log MMD (↓)                        | IS (↑)                              |
| SMC-ABC      | $8.21 \pm 2.36$                   | $-1.80 \pm 1.24$                   | $13.56 \pm 0.55$                   | $75.44 \pm 29.71$                  | $-4.48 \pm 0.55$                   | $81.69 \pm 7.73$                    |
| SNPE-A       | $1.46 \pm 1.72$                   | $-4.47 \pm 0.05$                   | $2.66 \pm 0.23$                    | $39.08 \pm 1.72$                   | $-4.55 \pm 0.21$                   | $34.74 \pm 3.68$                    |
| SNPE-B       | $27.66 \pm 23.83$                 | $-2.12 \pm 0.31$                   | $1.50 \pm 0.40$                    | $140.4 \pm 22.78$                  | $-1.83 \pm 0.13$                   | $19.43 \pm 0.93$                    |
| APT (SNPE-C) | $3.14 \pm 8.80$                   | $-3.27 \pm 0.71$                   | $7.39 \pm 4.48$                    | $69.04 \pm 93.53$                  | $-3.51 \pm 1.24$                   | $118.88 \pm 51.30$                  |
| AALR         | $0.89 \pm 0.12$                   | $-3.57 \pm 0.43$                   | $11.22 \pm 3.37$                   | $16.19 \pm 1.04$                   | $-6.81 \pm 0.68$                   | $208.91 \pm 4.33$                   |
| SNL          | $4.77 \pm 2.68$                   | $-2.53 \pm 0.54$                   | $5.34 \pm 3.43$                    | $40.40 \pm 11.84$                  | $-5.32 \pm 0.65$                   | $153.43 \pm 18.40$                  |
| SNL+PAR      | <b><math>0.55 \pm 0.79</math></b> | <b><math>-5.39 \pm 0.94</math></b> | <b><math>14.95 \pm 1.08</math></b> | <b><math>15.13 \pm 2.65</math></b> | <b><math>-6.51 \pm 0.86</math></b> | <b><math>211.85 \pm 4.07</math></b> |

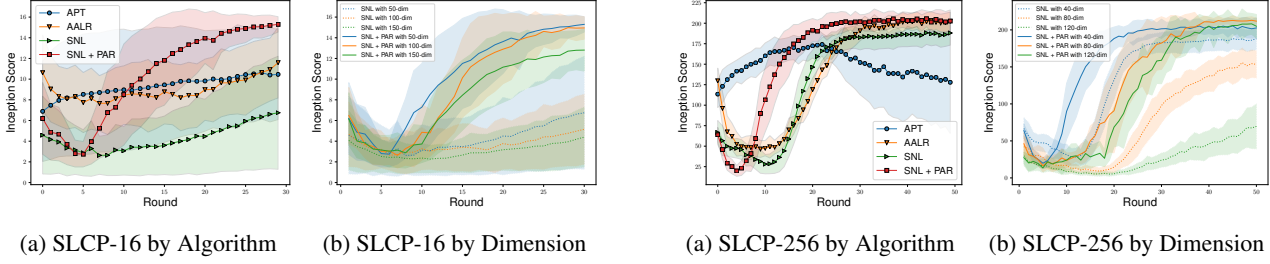


Figure 7. Comparison of Inception Score by round on SLCP-16 with 100 simulation budgets for each round on (a) baselines of 50-dimensional output and (b) varying dimensions.

less number of modes, eventually. APT struggles in this test because the estimation on  $Z(x; \phi)$  via an atomic proposal in APT becomes inaccurate on simulations with many modes. Analogous to SLCP-16, Figure 11 (b) illustrates the out-performance of the regularized SNL over the vanilla SNL. Figure 11 (b) indicates that the inference of SNL succeeds on low dimensional outputs, whereas the inference of SNL on high dimensional outputs fails given simulation budgets.

Table 1 shows the performances on SLCP-256. The regularized SNL performs better than the vanilla SNL and APT, but AALR beats the proposed method in the MMD score. However, AALR does not show any consistent performance if we compare SLCP-16 and SLCP-256 as well as the realistic

simulations in Table 2.

### 5.1.3. HYPERPARAMETER SELECTION

This section examines the effect of hyperparameter on inference. There are three strategies of hyperparameter selection. First, we experiment with a constant hyperparameter of  $\lambda$  to check if the inference performance indeed degrades due to the approximated nature in Theorem 4. Second, we experiment with exponentially decaying hyperparameters by the inference round in *Anneal by Round*. The hyperparameter at the initial round is set to five, and the exponent coefficient is chosen to make the hyperparameter at the last round to be 0.1. Third, we periodically decay the hyperparameter at

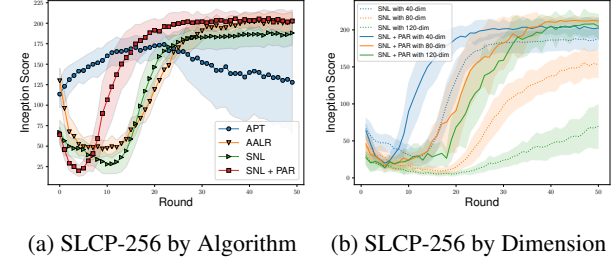
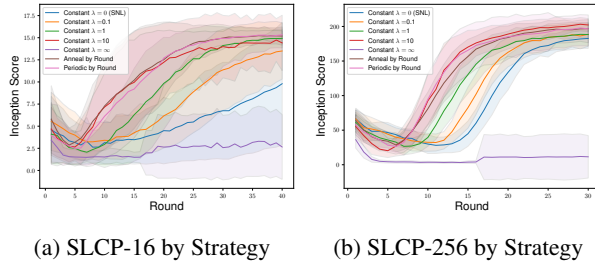


Figure 8. Comparison of Inception Score by round on SLCP-256 with 100 simulation budgets for each round on (a) baselines of 40-dimensional output and (b) varying dimensions.

**Table 2.** Comparison of negative log probability at groundtruth simulation inputs for M/G/1 model, Ricker model, and Poisson model. We run 40 rounds of inference for M/G/1, and 10 rounds of inference for Ricker and Poisson models with simulation budget per a round to be 20 for M/G/1 and 100 for Ricker and Poisson models.

| ALGORITHM    | M/G/1             |                   |                   | RICKER            |                   |                   | POISSON            |                    |                    |
|--------------|-------------------|-------------------|-------------------|-------------------|-------------------|-------------------|--------------------|--------------------|--------------------|
|              | OUTPUT DIMENSION  |                   |                   | OUTPUT DIMENSION  |                   |                   | OUTPUT DIMENSION   |                    |                    |
|              | 5                 | 20                | 100               | 13                | 20                | 100               | 25                 | 49                 | 361                |
| SMC-ABC      | 22.54±17.83       | 25.48±22.12       | 14.85±18.41       | 6.77±7.53         | 6.02±7.61         | 36.12±18.64       | 0.92±1.42          | 0.58±1.75          | 0.00±0.00          |
| SNPE-A       | 4.36±0.43         | 4.07±0.49         | 3.25±0.61         | 4.43±0.20         | 4.54±0.49         | 4.43±0.18         | 0.34±0.48          | 0.17±0.42          | -3.22±6.32         |
| SNPE-B       | 9.30±0.96         | 9.85±0.03         | 9.89±0.01         | 9.79±0.06         | 8.67±1.16         | 9.96±0.25         | 5.44±5.59          | 5.59±4.92          | 3.47±4.67          |
| APT (SNPE-C) | -3.49±0.97        | -2.27±7.14        | -3.01±1.82        | -0.62±0.98        | -0.24±3.86        | 4.13±6.16         | -11.61±1.93        | -11.61±2.50        | <b>-11.26±0.96</b> |
| AALR         | -1.18±0.59        | -1.69±0.51        | 1.14±2.08         | 4.10±0.51         | 1.82±0.77         | 3.15±2.55         | -6.36±1.66         | -6.25±0.92         | 0.28±0.66          |
| SNL          | -3.23±1.25        | -5.58±1.37        | -4.65±1.30        | -1.46±0.66        | -0.41±1.07        | 1.44±6.42         | -12.76±0.99        | -12.48±0.95        | -2.36±7.44         |
| SNL+PAR      | <b>-3.86±0.68</b> | <b>-6.36±0.78</b> | <b>-5.52±0.83</b> | <b>-1.78±0.89</b> | <b>-1.14±1.25</b> | <b>-0.48±0.70</b> | <b>-13.31±1.11</b> | <b>-13.61±0.83</b> | -5.33±4.33         |



**Figure 9.** Comparison of Inception Score by round upon various hyperparameter strategies on (a) SLCP-16 of 50-dimensional output (b) SLCP-256 of 40-dimensional output.

every round in *Periodic by Round*. We put the initial hyperparameter as five at each round, and the hyperparameter is decayed as to 0.1 after 100 epochs.

Figure 9 (a) presents the result on SLCP-16. The learning curve with the first strategy shows improving performance as the hyperparameter increases, but the performance dramatically degrades down when  $\lambda$  becomes the infinity. This correlation of the hyperparameter magnitude and the performance also occurs on SLCP-256 in Figure 9 (b), and we argue that the proposed regularization is robust on the hyperparameter selection as long as the hyperparameter lies on a moderate range,  $[0.1, 10]$ , though it is not guaranteed to be exact by Theorem 4. Also, Figure 9 shows that the strategies with annealing and periodic hyperparameters performs comparably to the best performance of the hyperparameter selection on both SLCP-16 and SLCP-256. This empirical result reduces the endeavor of hyperparameter selections, if we choose either annealing or periodic strategy.

## 5.2. Real-world Simulations

**M/G/1 Model** We test the M/G/1 model with various output dimensionalities. We define the summary statistics of the M/G/1 model as the equally dividend percentiles of the 1,000-dimensional inter-departure simulation raw output. With the varying dimension of the summary statistics, Table

2 presents the state-of-the-art inference on the posterior by SNL with PAR.

**Ricker Model** While we accept the need of summary statistics to mitigate unnecessary noise in simulation result for more accurate inference, we test the Ricker model in three cases. First, we consider 13 summary statistics (Wood, 2010) of the mean, the number of zeros, the autocovariances with lag up to five, the coefficients of a cubic regression of the ordered differences, and the coefficients of a least squares estimates. Second, we extract 20 equally distributed percentiles of the predicted simulation populations. Third, we infer the posterior *without* the summary statistics with 100-dimensional raw output. Table 2 presents that SNL with PAR gains a significant performance increment over the previous algorithms.

**Poisson Model** While the previous M/G/1 model and the Ricker model are temporal simulation models, the Poisson model is a time-independent simulation based on partial differential equations. We observe a vector of solution values at equally spaced pre-designated positions. Table 2 shows that SNL with PAR shows the second best in the high dimensional case, and SNL with PAR performs the best in the low and the middle cases.

## 6. Conclusion

This paper proposes a new regularization, PAR, which is applicable to the inference of the sequential neural likelihood. PAR is designed to pursue both learning the posterior detail as well as avoiding the overfitting, which could be seem contradictory with a glimpse. We show that these two objectives can coexist in a single neural network for the inference, as a unified structure. This coexistence is theoretically verified, and the empirical quality of the inferred posterior shows better fitness with increased mode captures by PAR. We expect this new regularization can simply, yet effectively change the practice of *likelihood-free inference*.

## References

Arjovsky, M., Chintala, S., and Bottou, L. Wasserstein gan. *arXiv preprint arXiv:1701.07875*, 2017.

Bachman, P., Hjelm, R. D., and Buchwalter, W. Learning representations by maximizing mutual information across views. In *Advances in Neural Information Processing Systems*, pp. 15535–15545, 2019.

Belghazi, M. I., Baratin, A., Rajeshwar, S., Ozair, S., Bengio, Y., Courville, A., and Hjelm, D. Mutual information neural estimation. In *International Conference on Machine Learning*, pp. 531–540. PMLR, 2018.

Caruana, R., Lawrence, S., and Giles, L. Overfitting in neural nets: Backpropagation, conjugate gradient, and early stopping. *Advances in neural information processing systems*, pp. 402–408, 2001.

Chen, X., Duan, Y., Houthooft, R., Schulman, J., Sutskever, I., and Abbeel, P. Infogan: Interpretable representation learning by information maximizing generative adversarial nets. *arXiv preprint arXiv:1606.03657*, 2016.

Danihelka, I., Lakshminarayanan, B., Uria, B., Wierstra, D., and Dayan, P. Comparison of maximum likelihood and gan-based training of real nvp. *arXiv preprint arXiv:1705.05263*, 2017.

Durkan, C., Bekasov, A., Murray, I., and Papamakarios, G. nflows: normalizing flows in PyTorch, November 2020. URL <https://doi.org/10.5281/zenodo.4296287>.

Greenberg, D., Nonnenmacher, M., and Macke, J. Automatic posterior transformation for likelihood-free inference. In *International Conference on Machine Learning*, pp. 2404–2414, 2019.

Grover, A., Dhar, M., and Ermon, S. Flow-gan: Combining maximum likelihood and adversarial learning in generative models. In *Proceedings of the AAAI Conference on Artificial Intelligence*, volume 32, 2018.

Gulrajani, I., Ahmed, F., Arjovsky, M., Dumoulin, V., and Courville, A. C. Improved training of wasserstein gans. In *Advances in neural information processing systems*, pp. 5767–5777, 2017.

Gutmann, M. U. and Corander, J. Bayesian optimization for likelihood-free inference of simulator-based statistical models. *The Journal of Machine Learning Research*, 17 (1):4256–4302, 2016.

He, K., Zhang, X., Ren, S., and Sun, J. Deep residual learning for image recognition. In *Proceedings of the IEEE conference on computer vision and pattern recognition*, pp. 770–778, 2016.

Hermans, J., Begy, V., and Louppe, G. Likelihood-free mcmc with amortized approximate ratio estimators. In *International Conference on Machine Learning*, 2020.

Hjelm, R. D., Fedorov, A., Lavoie-Marchildon, S., Grewal, K., Bachman, P., Trischler, A., and Bengio, Y. Learning deep representations by mutual information estimation and maximization. *arXiv preprint arXiv:1808.06670*, 2018.

Ke, L., Barnes, M., Sun, W., Lee, G., Choudhury, S., and Srinivasa, S. Imitation learning as  $f$ -divergence minimization. *arXiv preprint arXiv:1905.12888*, 2019.

Kim, D., Joo, W., Shin, S., and Moon, I.-C. Adversarial likelihood-free inference on black-box generator. *arXiv preprint arXiv:2004.05803*, 2020a.

Kim, D., Song, K., Kim, Y., Shin, Y., and Moon, I.-C. Sequential likelihood-free inference with implicit surrogate proposal. *arXiv preprint arXiv:2010.07604*, 2020b.

Lee, K. S., Tran, N.-T., and Cheung, N.-M. Infomax-gan: Improved adversarial image generation via information maximization and contrastive learning. In *Proceedings of the IEEE/CVF Winter Conference on Applications of Computer Vision*, pp. 3942–3952, 2020.

Lueckmann, J.-M., Goncalves, P. J., Bassetto, G., Oecal, K., Nonnenmacher, M., and Macke, J. H. Flexible statistical inference for mechanistic models of neural dynamics. In *Neural Information Processing Systems (NIPS 2017)*, 2018.

Nguyen, T., Le, T., Vu, H., and Phung, D. Dual discriminator generative adversarial nets. In *Advances in neural information processing systems*, pp. 2670–2680, 2017.

Nowozin, S., Cseke, B., and Tomioka, R. f-gan: Training generative neural samplers using variational divergence minimization. In *Advances in neural information processing systems*, pp. 271–279, 2016.

Papamakarios, G. and Murray, I. Fast  $\varepsilon$ -free inference of simulation models with bayesian conditional density estimation. In *Advances in Neural Information Processing Systems*, pp. 1028–1036, 2016.

Papamakarios, G., Sterratt, D., and Murray, I. Sequential neural likelihood: Fast likelihood-free inference with autoregressive flows. In *The 22nd International Conference on Artificial Intelligence and Statistics*, pp. 837–848, 2019.

Pascanu, R., Mikolov, T., and Bengio, Y. On the difficulty of training recurrent neural networks. In *International conference on machine learning*, pp. 1310–1318. PMLR, 2013.

Peng, J., Pedersoli, M., and Desrosiers, C. Mutual information deep regularization for semi-supervised segmentation. In *Medical Imaging with Deep Learning*, pp. 601–613. PMLR, 2020.

Poole, B., Alemi, A. A., Sohl-Dickstein, J., and Angelova, A. Improved generator objectives for gans. *arXiv preprint arXiv:1612.02780*, 2016.

Poole, B., Ozair, S., Van Den Oord, A., Alemi, A., and Tucker, G. On variational bounds of mutual information. In *International Conference on Machine Learning*, pp. 5171–5180. PMLR, 2019.

Salimans, T., Goodfellow, I., Zaremba, W., Cheung, V., Radford, A., and Chen, X. Improved techniques for training gans. In *Advances in neural information processing systems*, pp. 2234–2242, 2016.

Shao, J., Wang, Q., and Liu, F. Learning to sample: an active learning framework. In *2019 IEEE International Conference on Data Mining (ICDM)*, pp. 538–547. IEEE, 2019.

Sisson, S. A., Fan, Y., and Tanaka, M. M. Sequential monte carlo without likelihoods. *Proceedings of the National Academy of Sciences*, 104(6):1760–1765, 2007.

Sriperumbudur, B. K., Gretton, A., Fukumizu, K., Schölkopf, B., and Lanckriet, G. R. Hilbert space embeddings and metrics on probability measures. *The Journal of Machine Learning Research*, 11:1517–1561, 2010.

Tejero-Cantero, A., Boelts, J., Deistler, M., Lueckmann, J.-M., Durkan, C., Gonçalves, P. J., Greenberg, D. S., and Macke, J. H. sbi: A toolkit for simulation-based inference. *Journal of Open Source Software*, 5(52):2505, 2020. doi: 10.21105/joss.02505. URL <https://doi.org/10.21105/joss.02505>.

Wood, S. N. Statistical inference for noisy nonlinear ecological dynamic systems. *Nature*, 466(7310):1102–1104, 2010.

Zhang, M., Bird, T., Habib, R., Xu, T., and Barber, D. Variational f-divergence minimization. *arXiv preprint arXiv:1907.11891*, 2019.

Zhao, S., Song, J., and Ermon, S. Infovae: Information maximizing variational autoencoders. *arXiv preprint arXiv:1706.02262*, 2017.

## A. Simulations

### A.1. Tractable Simulations

#### A.1.1. SLCP-16

The Simple-Likelihood-and-Complex-Posterior-16 (SLCP-16) (Kim et al., 2020b) is a simulation with 16 modes in its posterior distribution. The model input parameter is five-dimensional and the model output dimension is a variable to choose. The model is defined by

$$\begin{aligned} \theta_i &\sim U(-3, 3) \quad \text{for } i = 1, \dots, 5 \\ \mu_\theta &= (\theta_1^2, \theta_2^2) \\ \sigma_1 &= \theta_3^2, \quad \sigma_2 = \theta_4^2, \quad \rho = \tanh(\theta_5) \\ \Sigma_\theta &= \begin{pmatrix} \sigma_1^2 & \rho\sigma_1\sigma_2 \\ \rho\sigma_1\sigma_2 & \sigma_2^2 \end{pmatrix} \\ x &= x_1 \oplus \dots \oplus x_n \quad \text{with } x_i \sim \mathcal{N}(\mu_\theta, \Sigma_\theta), \end{aligned}$$

where  $\oplus$  denotes the vector concatenation. As the name suggests, the likelihood function is a simple Gaussian distribution, whereas the posterior is complex with 16 modes. Also, we can vary the output dimension of SLCP-16 by controlling  $n$ . The prior distribution of the model is the uniform distribution on  $[-3, 3]^5$ . The true parameter becomes  $(\theta_1^*, \theta_2^*, \theta_3^*, \theta_4^*, \theta_5^*) = (1.5, -2.0, -1.0, -0.9, 0.6)$ .

#### A.1.2. SLCP-256

The Simple-Likelihood-and-Complex Posterior-256 (SLCP-256) (Kim et al., 2020b) is a simulation with 256 modes in its posterior distribution. The model input parameter is eight-dimensional, and the model output is a variable to choose. The model is defined by

$$\begin{aligned} \theta_i &\sim U(-3, 3) \quad \text{for } i = 1, \dots, 8 \\ x &= x_1 \oplus \dots \oplus x_n \quad \text{with } x_j \sim \mathcal{N}(\theta^2, \mathbf{I}), \end{aligned}$$

where  $n$  is a control parameter for output dimension. The prior distribution of the model is the uniform distribution on  $[-3, 3]^8$ . The true parameter configuration is as  $(\theta_1^*, \theta_2^*, \theta_3^*, \theta_4^*, \theta_5^*, \theta_6^*, \theta_7^*, \theta_8^*) = (1.5, 2.0, 1.3, 1.2, 1.8, 2.5, 1.6, 1.1)$ .

### A.2. Real-world Simulations

We introduce different types of simulations in their modeling framework.

#### A.2.1. M/G/1 MODEL

The M/G/1 model is a discrete-event simulation that models the state transition of a waiting line with a single server according to the sampling-based discrete events (customer arrive). This model is highly stochastic, and the likelihood,  $p(x|\theta)$ , is supported on a expansive area. Therefore, the

likelihood-free inference fails if the observation is a singleton unless we filter the raw output by a set of summary statistics. Although there could be alternative choices for the summary statistics, we choose equally dividend percentiles. We choose this elementary statistics in order to minimize the domain knowledge in the selection of the summary statistics.

Suppose the arrival of customers ( $v$ ) is modeled by a Poisson process, and the service time ( $s$ ) is modeled by a uniform distribution. Then the finish time is calculated by

$$\begin{aligned} s(i) &\sim U(\theta_1, \theta_1 + \theta_2), \\ v(i) - v(i-1) &\sim \text{Exp}(\theta_3), \\ d(i) - d(i-1) &= s(i) + \max(0, v(i) - d(i-1)). \end{aligned}$$

We follow Papamakarios et al. (2019) to set the observation as a trajectory of  $\{d(i) - d(i-1)\}_{i=1}^I$ . We determine  $I$  to be 1,000. The model has three input parameters,  $(\theta_1, \theta_2, \theta_3)$ , that describe the waiting line. The service time is determined by a uniform distribution on  $[\theta_1, \theta_1 + \theta_2]$ , and  $\theta_3$  determines the customer arrival time. We consider a uniform prior distribution on  $[0, 10] \times [0, 10] \times [0, 1/3]$ . The true parameter configuration is given by  $(\theta_1^*, \theta_2^*, \theta_3^*) = (1, 4, 0.2)$ .

#### A.2.2. RICKER MODEL

The Ricker model is a system dynamics simulation that models the animal population that is latent. For example, the number of fish in the ocean cannot be observed, but it is extremely important to predict it in order to keep the sustainability of the environment. While the underlying animal population follows a simple equation, the observed population at each time is based on a sampling from a Poisson distribution, which creates the stochasticity in this model.

The underlying population is described as a nonlinear autoregressive equation by

$$\log N_t = \log r + \log N_{t-1} - N_{t-1} + \sigma e_t,$$

where  $N_t$  is the size of the animal population at time  $t$ , and  $e_t$  is a standard Gaussian random variable. The population starts from  $N_0 = 0$ . Here,  $\log r$  determines the population growth size, and  $\sigma$  represents the randomness of the population growth.

Additionally, the observation model follows a Poisson distribution with

$$y_t \sim \text{Poisson}(\phi N_t),$$

where  $\phi$  is a scaling parameters. The model output is  $\{y_t\}_{t=1}^T$  with  $T = 100$  timesteps.

We extract two set of summary statistics. The first set consists of 13 summary statistics (Wood, 2010): 1) the mean

population,  $\bar{y} = \frac{1}{T} \sum_{t=1}^T y_t$ ; 2) the number of zeros observed; 3) the coefficients,  $\beta_1$  and  $\beta_2$ , of the autoregression  $y_{t+1}^{0.3} = \beta_1 y_t^{0.3} + \beta_2 y_t^{0.6} + e_t$ ; 4) the coefficients of the cubic regression of the ordered differences,  $y_t - y_{t-1}$ , on their observed values; and 5) the autocovariances up to lag five. The choice of these summary statistics depends on domain knowledge. The other set of summary statistics is the equally distributed percentiles.

We consider a uniform prior on  $[0, 5] \times [0, 1] \times [0, 15]$ , and the true parameter to be  $(\log r^*, \sigma^*, \phi^*) = (3.8, 0.3, 10)$ .

#### A.2.3. POISSON MODEL

The Poisson model is a second-order partial differential equation. The generalized Laplace operator in the generalized Poisson equation models the random walk effect with the nonlinear diffusion coefficient ( $q$ ) that could explain a porous material heat diffusivity. We assume a mixed boundary condition, which combines the Dirichlet boundary condition on the top and the bottom boundaries, and a Neumann boundary condition on the left and the right boundaries:

$$\begin{aligned} -\nabla \cdot (q \nabla u) &= 1 && \text{in } \Omega \\ u &= 5 && \text{on } \partial\Omega_T \\ u &= 0 && \text{on } \partial\Omega_B \\ \nabla u \cdot n &= -10e^{-(y-0.5)^2} && \text{on } \partial\Omega_L \\ \nabla u \cdot n &= 1 && \text{on } \partial\Omega_R, \end{aligned}$$

where  $\partial\Omega_T, \partial\Omega_B, \partial\Omega_L$  and  $\partial\Omega_R$  are the top, bottom, left, and right sides of the unit square domain,  $\Omega = [0, 1]^2$ , respectively. The Dirichlet condition on the top and the bottom sides indicate that the temperature is fixed throughout the boundaries. The Neumann condition on the right side means there exist a heat influx. The Neumann condition on the left side means the heat is dissipating outwardly. The Poisson model describes the stationary heat diffusion of the time-dependent heat equation. The nonlinear diffusivity is defined by

$$q(x, y) = \begin{cases} \theta_1 & \text{if } x \leq 0.5 \wedge y \leq 0.5 \\ \theta_2 & \text{if } x \leq 0.5 \wedge y > 0.5 \\ \theta_3 & \text{if } x > 0.5 \wedge y \leq 0.5 \\ \theta_4 & \text{if } x > 0.5 \wedge y > 0.5 \end{cases}$$

We fine the weak solution  $u \in V$  of the variational form given by

$$a(u, v) = L(v) \quad \forall v \in \hat{V},$$

where  $\hat{V}$  is the space of test functions, i.e.  $C_c^\infty(\Omega)$ ;  $V$  is the space of  $C^\infty(\Omega)$  that satisfies the top and the bottom

Dirichlet boundary conditions; and

$$\begin{aligned} a(u, v) &= \int_{\Omega} q(\mathbf{x}) \nabla u(\mathbf{x}) \cdot \nabla v(\mathbf{x}) d\mathbf{x} \\ L(v) &= \int_{\partial\Omega_L} -10e^{-(y-0.5)^2} v(\mathbf{x}) ds + \int_{\partial\Omega_R} v(\mathbf{x}) ds \\ &+ \int_{\Omega} v(\mathbf{x}) d\mathbf{x}. \end{aligned}$$

The observation is a vector of solution values  $\{u_1^*, \dots, u_D^*\}$  at equally spaced pre-designated positions,  $x_1, \dots, x_D$ , respectively. We use the uniform prior on  $[0, 1]^4$ , and the true parameter as  $(\theta_1^*, \theta_2^*, \theta_3^*, \theta_4^*) = (0.1, 0.9, 0.6, 0.2)$ .

### A.3. Toy Simulations

#### A.3.1. SIMULATION OF FIGURE 1

We use a simulation model with

$$\begin{aligned} \theta_i &\sim U(0, 1) \quad \text{for } i = 1, 2 \\ x &\sim \mathcal{N}([\cos 5\pi\theta_1, \cos 5\pi\theta_2]^T, 0.1\mathbf{I}). \end{aligned}$$

With the observation of  $x_o = [0, 0]^T$ , the true posterior attains equally spaced 25 periodic modalities. Surprisingly, the vanilla SNL fails at capturing multi-modalities of this low-dimensional simulation model.

#### A.3.2. SIMULATION OF FIGURE 5

The true likelihood is  $p(x_1) = \mathcal{N}(x_1; 0, 1)$  and  $p(x_2|x_1) = \mathcal{N}(x_2; x_1, 1)$ , and the modeled likelihood is defined by  $q(x_1) = \mathcal{N}(x_1; 0, \theta_1^2)$  and  $q(x_2|x_1) = \mathcal{N}(x_2; x_1, \theta_2^2)$ , where  $\theta_1$  and  $\theta_2$  are the modeling parameters. Here, the marginal distribution becomes  $q(x_2) = \mathcal{N}(x_2; 0, \theta_1^2 + \theta_2^2)$ .

This simple simulation model attains the tractable divergence formulas. We compute the forward KL divergence as follows.

$$\begin{aligned} D_{KL}(p, q) &= \int \int p(x_1, x_2) \log \frac{p(x_1, x_2)}{q(x_1, x_2)} dx_1 dx_2 \\ &= - \int \int p(x_1, x_2) \log q(x_1, x_2) dx_1 dx_2 - \mathbb{H}(p) \\ &= - \int \int p(x_1, x_2) \\ &\quad \log \left[ \frac{1}{\theta_1 \theta_2} e^{-\frac{x_1^2}{2\theta_1^2} - \frac{(x_2 - x_1)^2}{2\theta_2^2}} \right] dx_1 dx_2 - \mathbb{H}(p). \end{aligned}$$

Here, the entropy of  $p$ ,  $\mathbb{H}(p)$ , is constant along the optimization of  $q$ . From

$$-\frac{x_1^2}{2\theta_1^2} - \frac{(x_2 - x_1)^2}{2\theta_2^2} = -\frac{(\theta_1^2 + \theta_2^2)x_1^2 - 2\theta_1^2 x_1 x_2 + \theta_1^2 x_2^2}{2\theta_1^2 \theta_2^2},$$

the forward KL calculation is decomposed by five terms,

$D_{KL}(p, q) = (1) + (2) + (3) + (4) + (5)$ , with

$$\begin{aligned} (1) &= \log \theta_1 + \log \theta_2, \\ (2) &= \frac{\theta_1^2 + \theta_2^2}{2\theta_1^2 \theta_2^2} \int \int x_1^2 p(x_1, x_2) dx_1 dx_2 \\ &= \frac{\theta_1^2 + \theta_2^2}{2\theta_1^2 \theta_2^2} \int x_1^2 p(x_1) dx_1 \\ &= \frac{\theta_1^2 + \theta_2^2}{2\theta_1^2 \theta_2^2}, \\ (3) &= -\frac{1}{\theta_2^2} \int \int x_1 x_2 p(x_1, x_2) dx_1 dx_2 \\ &= -\frac{1}{\theta_2^2}, \\ (4) &= \frac{1}{2\theta_2^2} \int \int x_2^2 p(x_1, x_2) dx_1 dx_2 \\ &= \frac{1}{2\theta_2^2} \int x_2^2 p(x_2) dx_2 \\ &= \frac{1}{\theta_2^2}, \\ (5) &= -\mathbb{H}(p). \end{aligned}$$

Therefore, the closed-form of the forward KL divergence is

$$D_{KL}(p, q) = \log \theta_1 + \log \theta_2 + \frac{\theta_1^2 + \theta_2^2}{2\theta_1^2 \theta_2^2} - \mathbb{H}(p).$$

Also, the reverse KL divergence becomes

$$D_{KL}(q||p) = \int \int q(x_1, x_2) \log \frac{q(x_1, x_2)}{p(x_1, x_2)} dx_1 dx_2,$$

where

$$\frac{q(x_1, x_2)}{p(x_1, x_2)} = \frac{1}{\theta_1 \theta_2} e^{-\frac{x_1^2}{2\theta_1^2} - \frac{(x_2 - x_1)^2}{2\theta_2^2} + \frac{x_1^2}{2} + \frac{(x_2 - x_1)^2}{2}}$$

Analogously, the reverse KL divergence is decomposed by five terms

$$D_{KL}(q, p) = (1) + (2) + (3) + (4) + (5),$$

where

$$\begin{aligned}
 (1) &= -(\log \theta_1 + \log \theta_2) \int \int q(x_1, x_2) dx_1 dx_2 \\
 &= -(\log \theta_1 + \log \theta_2), \\
 (2) &= -\frac{1}{2\theta_1^2} \int \int x_1^2 q(x_1, x_2) dx_1 dx_2 \\
 &= -\frac{1}{2\theta_1^2} \int x_1^2 q(x_1) dx_1 \\
 &= -\frac{1}{2}, \\
 (3) &= -\frac{1}{2\theta_2^2} \int \int (x_2 - x_1)^2 q(x_1, x_2) dx_1 dx_2 \\
 &= -\frac{1}{2\theta_2^2} \int q(x_1) \int (x_2 - x_1)^2 q(x_2|x_1) dx_2 dx_1 \\
 &= -\frac{1}{2\theta_2^2} \int q(x_1) \theta_2^2 dx_1 \\
 &= -\frac{1}{2} \\
 (4) &= \frac{1}{2} \int \int x_1^2 q(x_1, x_2) dx_1 dx_2 \\
 &= \frac{\theta_1^2}{2} \\
 (5) &= \frac{1}{2} \int \int (x_2 - x_1)^2 q(x_1, x_2) dx_1 dx_2 \\
 &= \frac{\theta_2^2}{2}
 \end{aligned}$$

Therefore, the closed-form of the reverse KL divergence becomes

$$D_{KL}(q, p) = -\log \theta_1 - \log \theta_2 + \frac{\theta_1^2 + \theta_2^2}{2} - 1.$$

The mutual information becomes

$$\begin{aligned}
 \mathbb{I}(X_1, X_2) &= \int \int q(x_1, x_2) \log \frac{q(x_1, x_2)}{q(x_1)q(x_2)} dx_1 dx_2 \\
 &= \int \int q(x_1)q(x_2|x_1) \log \frac{q(x_2|x_1)}{q(x_2)} dx_1 dx_2 \\
 &= \int \int \mathcal{N}(x_1; 0, \theta_1^2) \mathcal{N}(x_2; x_1, \theta_2^2) \\
 &\quad \log \frac{\mathcal{N}(x_2; x_1, \theta_2^2)}{\mathcal{N}(x_2; 0, \theta_1^2 + \theta_2^2)} dx_1 dx_2.
 \end{aligned}$$

Here, we have

$$\frac{\mathcal{N}(x_2; x_1, \theta_2^2)}{\mathcal{N}(x_2; 0, \theta_1^2 + \theta_2^2)} = \frac{\sqrt{\theta_1^2 + \theta_2^2}}{\theta_2} e^{\frac{-(\theta_1^2 + \theta_2^2)x_1^2 + 2(\theta_1^2 + \theta_2^2)x_1x_2 - \theta_2^2x_2^2}{2\theta_2^2(\theta_1^2 + \theta_2^2)}}$$

Therefore,  $\mathbb{I}(X_1, X_2)$  is decomposed by

$$\mathbb{I}(X_1, X_2) = (1) + (2) + (3) + (4) + (5),$$

with

$$\begin{aligned}
 (1) &= \frac{1}{2} \log(\theta_1^2 + \theta_2^2) \int \int q(x_1, x_2) dx_1 dx_2 \\
 &= \frac{1}{2} \log(\theta_1^2 + \theta_2^2), \\
 (2) &= -\log \theta_2, \\
 (3) &= -\frac{1}{2\theta_2^2} \int \int x_1^2 q(x_1, x_2) dx_1 dx_2 \\
 &= -\frac{1}{2\theta_2^2} \int x_1^2 q(x_1) dx_1 \\
 &= -\frac{1}{2\theta_2^2} \int x_1^2 \mathcal{N}(x_1; 0, \theta_1^2) dx_1 \\
 &= -\frac{\theta_1^2}{2\theta_2^2}, \\
 (4) &= \frac{1}{\theta_2^2} \int \int x_1 x_2 q(x_1, x_2) dx_1 dx_2 \\
 &= \frac{1}{\theta_2^2} \int x_1 q(x_1) \int x_2 q(x_2|x_1) dx_2 dx_1 \\
 &= \frac{1}{\theta_2^2} \int x_1 q(x_1) \left[ \int (x_2 - x_1) \mathcal{N}(x_2; x_1, \theta_2^2) dx_2 \right. \\
 &\quad \left. + \int x_1 \mathcal{N}(x_2; x_1, \theta_2^2) dx_2 \right] dx_1 \\
 &= \frac{1}{\theta_2^2} \int x_1^2 q(x_1) dx_1 \\
 &= \frac{\theta_1^2}{\theta_2^2}, \\
 (5) &= -\frac{\theta_1^2}{2\theta_2^2(\theta_1^2 + \theta_2^2)} \int \int x_2^2 q(x_1, x_2) dx_1 dx_2 \\
 &= -\frac{\theta_1^2}{2\theta_2^2(\theta_1^2 + \theta_2^2)} \int x_2^2 q(x_2) dx_2 \\
 &= -\frac{\theta_1^2}{2\theta_2^2},
 \end{aligned}$$

Therefore, the closed-form of the mutual information becomes

$$\mathbb{I}(X_1, X_2) = \frac{1}{2} \log(\theta_1^2 + \theta_2^2) - \log \theta_2.$$

## B. Proof of Theorems

**Theorem 3.** Suppose  $\hat{F}(\psi)$  is defined to be  $-\mathbb{E}_{\tilde{p}(\theta)q_\psi(x|\theta)} [\log \tilde{p}(\theta|x)]$ , then  $\hat{F}(\psi)$  is decomposed into  $\hat{F}(\psi) = \hat{F}^{(1)}(\psi) + F^{(2)}(\psi) + \text{const.}$  with

$$\hat{F}^{(1)}(\psi) = D_{KL}(\tilde{q}_\psi(x)\tilde{q}_\psi(\theta|x), \tilde{q}_\psi(x)\tilde{p}(\theta|x))$$

$$F^{(2)}(\psi) = -\mathbb{I}(\Theta, X).$$

*Proof.* The regularization becomes

$$\begin{aligned}
 \hat{F}(\psi) &= -\mathbb{E}_{\tilde{p}(\theta)q_\psi(x|\theta)}[\log \tilde{p}(\theta|x)] \\
 &= -\int \int \tilde{p}(\theta)q_\psi(x|\theta) \log \tilde{p}(\theta|x) d\theta dx \\
 &= \int \int \tilde{p}(\theta)q_\psi(x|\theta) \log \frac{\tilde{p}(\theta)q_\psi(x|\theta)}{\tilde{p}(\theta|\tilde{q}_\psi(x))} d\theta dx \\
 &\quad + \int \int \tilde{p}(\theta)q_\psi(x|\theta) \log \frac{\tilde{q}_\psi(x)}{\tilde{p}(\theta)q_\psi(x|\theta)} d\theta dx \\
 &= D_{KL}(\tilde{p}(\theta)q_\psi(x|\theta), \tilde{q}_\psi(x)\tilde{p}(\theta|x)) \\
 &\quad - D_{KL}(\tilde{p}(\theta)q_\psi(x|\theta), \tilde{p}(\theta)\tilde{q}_\psi(x)) \\
 &\quad - \int \tilde{p}(\theta) \log \tilde{p}(\theta) d\theta \\
 &= \hat{F}^{(1)}(\psi) + \hat{F}^{(2)}(\psi) + \mathbb{H}(\tilde{p}),
 \end{aligned}$$

since  $\mathbb{I}(\Theta, X) = D_{KL}(\tilde{p}(\theta)q_\psi(x|\theta), \tilde{p}(\theta)\tilde{q}_\psi(x))$ .  $\square$

**Theorem 4.** Suppose  $p(\theta, x)$  and  $p(\theta)$  are bounded on a positive interval,  $\tilde{p}(\theta)$  is bounded below, and  $q_\psi(\theta, x)$  is uniformly upper bounded on  $\psi$ . Then the optimization problem  $\arg \min_{q_\psi} \mathcal{L}_\phi^\lambda(\psi)$  attains the unique solution of

$$q_{\psi^*}^\lambda(x|\theta) = \frac{p(x|\theta)}{c(\theta) - \lambda \log \tilde{q}_\phi(\theta|x)},$$

where  $c(\theta)$  is a constant with respect to  $x$  that makes  $q_{\psi^*}^\lambda(x|\theta)$  a distribution in  $x$ -space.

Before we prove Theorem 4, we need a lemma.

**Lemma 1.** Suppose a measurable function  $f(x, y)$  is bounded below. Then,  $\int \int u(x, y)f(x, y)dx dy = 0$  holds for all measurable  $u$  with  $\int u(x, y)dx = 0$  for all  $y \in Y$  if and only if  $f(x, y) = c(y)$  for some measurable function  $c$ .

*Proof.* Without loss of generality, we assume  $f(x, y)$  to be nonnegative.

( $\Rightarrow$ ) Let  $\eta$  be positive and satisfy  $\int \eta(x) = 1$ . If we define  $u_0(x, y)$  to be

$$u_0(x, y) := \eta(x)f(x, y) - \eta(x) \int \eta(x')f(x', y)dx',$$

the integration of  $u_0(x, y)$  over  $x$  becomes

$$\begin{aligned}
 \int u_0(x, y)dx &= \int \eta(x)f(x, y)dx \\
 &\quad - \int \eta(x) \int \eta(x')f(x', y)dx' dx \\
 &= \int \eta(x)f(x, y)dx - \int \eta(x')f(x', y)dx' \\
 &= 0.
 \end{aligned}$$

Therefore, we have

$$\begin{aligned}
 0 &= \int \int u_0(x, y)f(x, y)dx dy \\
 &= \int \int \eta(x)f^2(x, y)dx dy \\
 &\quad - \int \left( \int \eta(x)f(x, y)dx \right) \left( \int \eta(x')f(x', y)dx' \right) dy \\
 &= \int \int \eta(x)f^2(x, y)dx dy - \int \left( \int \eta(x)f(x, y)dx \right)^2 dy.
 \end{aligned}$$

On the other hand,

$$\begin{aligned}
 &\left( \int \left( \int \eta(x)f(x, y)dx \right)^2 dy \right)^{1/2} \\
 &\leq \int \left( \int \eta^2(x)f^2(x, y)dy \right)^{1/2} dx
 \end{aligned} \tag{5}$$

$$\begin{aligned}
 &= \int \eta(x) \left( \int f^2(x, y)dy \right)^{1/2} dx \\
 &\leq \left( \int \eta(x)dx \right)^{1/2} \left( \int \eta(x) \int f^2(x, y)dy dx \right)^{1/2} \\
 &= \left( \int \int \eta(x)f^2(x, y)dy dx \right)^{1/2},
 \end{aligned} \tag{6}$$

where inequality 5 holds from Minkowski inequality, and inequality 6 holds from Hölder's inequality. Therefore, we have

$$0 = \int \int u_0(x, y)f(x, y)dx dy \geq 0,$$

and the equality holds if and only if the equality conditions of Minkowski inequality and Hölder's inequality hold.

The equality condition of Minkowski inequality is

$$\eta(x)f(x, y) = f_1(x)f_2(y), \tag{7}$$

for some nonnegative measurable functions  $f_1$  and  $f_2$ . Also, the equality conditions of Hölder's inequality is

$$\eta^{1/2}(x) \left( \int f^2(x, y)dy \right)^{1/2} = c\eta^{1/2}(x), \tag{8}$$

for some constant  $c \geq 0$ . Therefore, from Eq. 8, we have

$$\int f^2(x, y)dy = c, \tag{9}$$

for some  $c \geq 0$  (we use abuse of notation for  $c$ ), and by plugging Eq. 7 into Eq. 9, we have

$$f_1^2(x) = c\eta^2(x),$$

for some  $c \geq 0$ . Therefore,  $f(x, y) = cf_2(y)$  for some nonnegative measurable function  $f_2$  and some constant  $c \geq 0$ .

( $\Leftarrow$ ) Assume  $f(x, y) = c(y)$ , then for any  $u$  with  $\int u(x, y)dx = 0$  for all  $y \in Y$ , we have

$$\begin{aligned} & \int \int u(x, y)f(x, y)dxdy \\ &= \int \int u(x, y)c(y)dxdy \\ &= \int c(y) \left( \int u(x, y)dx \right) dy \\ &= 0. \end{aligned}$$

□

*Proof of Theorem 4.* For the proof of theorem, let us define  $\mathcal{L}_\phi^\lambda(q_\psi) := \mathcal{L}_\phi^\lambda(\psi)$ . Also, suppose  $u(\theta, x)$  is a function of  $(\theta, x)$  that satisfies  $\int u(\theta, x)dx = 0$  for any  $\theta$ . Then, the function of  $(q + \epsilon r)(x|\theta) := q(x|\theta) + \epsilon u(\theta, x)$  becomes a distribution on  $x$  for any  $\theta$ .

The difference  $\mathcal{L}_\phi^\lambda(q + \epsilon u) - \mathcal{L}_\phi^\lambda(q)$  becomes

$$\begin{aligned} & \mathcal{L}_\phi^\lambda(q + \epsilon u) - \mathcal{L}_\phi^\lambda(q) \\ &= \mathcal{L}_{SNL}(q + \epsilon u) - \mathcal{L}_{SNL}(q) \quad (10) \\ &+ \hat{F}_\phi(q + \epsilon u) - \hat{F}_\phi(q). \quad (11) \end{aligned}$$

Then, the first difference of Eq. 10 becomes

$$\begin{aligned} \text{Eq. 10} \\ &= - \int \int \tilde{p}(\theta)p(x|\theta) \log (q(x|\theta) + \epsilon u(\theta, x)) d\theta dx \\ &+ \int \int \tilde{p}(\theta)p(x|\theta) \log q(x|\theta) d\theta dx \\ &= - \int \int \tilde{p}(\theta)p(x|\theta) \log \frac{q(x|\theta) + \epsilon u(\theta, x)}{q(x|\theta)} d\theta dx \\ &= - \int \int \tilde{p}(\theta)p(x|\theta) \log \left( 1 + \epsilon \frac{u(\theta, x)}{q(x|\theta)} \right) d\theta dx \\ &= -\epsilon \int \int \tilde{p}(\theta)u(\theta, x) \frac{p(x|\theta)}{q(x|\theta)} d\theta dx + o(\epsilon), \quad (12) \end{aligned}$$

and the second difference of Eq. 11 becomes

$$\begin{aligned} \text{Eq. 11} \\ &= -\lambda \int \int \tilde{p}(\theta)(q(x|\theta) + \epsilon u(\theta, x)) \log \tilde{q}_\phi(\theta|x) d\theta dx \\ &+ \lambda \int \int \tilde{p}(\theta)q(x|\theta) \log \tilde{q}_\phi(\theta|x) d\theta dx \\ &= -\epsilon \lambda \int \int \tilde{p}(\theta)u(\theta, x) \log \tilde{q}_\phi(\theta|x) d\theta dx. \quad (13) \end{aligned}$$

Therefore, from Eq. 12 and Eq. 13, we have

$$\begin{aligned} & \mathcal{L}_\phi^\lambda(q + \epsilon u) - \mathcal{L}_\phi^\lambda(q) \\ &= -\epsilon \int \int \tilde{p}(\theta)u(\theta, x) \left( \frac{p(x|\theta)}{q(x|\theta)} + \lambda \log \tilde{q}_\phi(\theta|x) \right) d\theta dx \\ &+ o(\epsilon). \end{aligned}$$

The distribution of  $q$  becomes the optimal solution of  $\arg \min_q \mathcal{L}_\phi^\lambda(q)$  if and only if the Frechet derivative of  $\mathcal{L}_\phi^\lambda(q)$  becomes zero, which is equivalent with

$$\int \tilde{p}(\theta) \int u(\theta, x) \left( \frac{p(x|\theta)}{q(x|\theta)} + \lambda \log \tilde{q}_\phi(\theta|x) \right) dx d\theta = 0, \quad (14)$$

for all  $u(\theta, x)$  with  $\int u(\theta, x)dx = 0, \forall \theta \in \Theta$ . If we define  $\bar{u}(\theta, x) := \tilde{p}(\theta)u(\theta, x)$ , then Eq. 14 is equivalent to

$$\int \int \bar{u}(\theta, x) \left( \frac{p(x|\theta)}{q(x|\theta)} + \lambda \log \tilde{p}(\theta|x) \right) dx d\theta = 0,$$

for all  $\bar{u}(\theta, x)$  with  $\int \bar{u}(\theta, x)dx = 0, \forall \theta \in \Theta$ .

From assumptions,  $\frac{p(x|\theta)}{q(x|\theta)} = \frac{p(\theta, x)}{q(\theta, x)}$  is bounded below because the denominator,  $q(\theta, x)$  is bounded above and  $p(\theta, x)$  is bounded below. Also,  $\tilde{p}(x) = \int \tilde{p}(\theta)p(x|\theta)d\theta = \int \tilde{p}(\theta) \frac{p(\theta, x)}{p(\theta)} d\theta \leq \sup_{(\theta, x)} \frac{p(\theta, x)}{p(\theta)}$ , and  $\tilde{p}(\theta)$  is bounded below by a positive constant. Hence,  $\tilde{p}(\theta|x) = \frac{\tilde{p}(\theta)p(\theta, x)}{p(\theta)\tilde{p}(x)}$  is bounded below. Thus, we conclude that  $\frac{p(x|\theta)}{q(x|\theta)} + \lambda \log \tilde{p}(\theta|x)$  is bounded below, and we could apply Lemma 1. Therefore, the optimal solution of  $\arg \min_q \mathcal{L}_\phi^\lambda(q)$  exists to be

$$q^*(x|\theta) = \frac{p(x|\theta)}{c(\theta) - \lambda \log \tilde{p}(\theta|x)}.$$

Note that  $c(\theta) = \frac{p(x|\theta)}{q(x|\theta)} + \lambda \log \tilde{p}(\theta|x) > \lambda \log \tilde{p}(\theta|x)$ , so  $c(\theta) - \lambda \log \tilde{p}(\theta|x) > 0$ , and the optimal solution  $q^*$  is well defined.

Let us assume there exists a function  $\hat{c}(\theta)$  with  $c(\theta) \neq \hat{c}(\theta)$  for some  $\theta$  such that

$$\hat{q}^*(x|\theta) = \frac{p(x|\theta)}{\hat{c}(\theta) - \lambda \log \tilde{p}(\theta|x)}.$$

If  $c(\theta) > \hat{c}(\theta)$  at  $\theta$ , then

$$\begin{aligned} 1 &= \int q^*(x|\theta) dx \\ &= \int \frac{p(x|\theta)}{c(\theta) - \lambda \log \tilde{p}(\theta|x)} dx \\ &< \int \frac{p(x|\theta)}{\hat{c}(\theta) - \lambda \log \tilde{p}(\theta|x)} dx \\ &= \int \hat{q}^*(x|\theta) dx \\ &= 1, \end{aligned}$$

Table 3. Comparison of Complex Analysis

| Algorithm | Learning with (Regularized) Loss | Additional Posterior Learning |
|-----------|----------------------------------|-------------------------------|
| APT       | $O(rNEB_1)$                      | —                             |
| AALR      | $O(rNEB_2)$                      | —                             |
| SNL       | $O(rNEB_3)$                      | —                             |
| SNL+PAR   | $O(rNE(B_1 + B_3))$              | $O(rNEB_1)$                   |

which is a contradiction. Therefore, the optimal solution is unique.  $\square$

## C. Complexity Analysis

Table 3 analyzes the time complexity at the  $r$ -th round of the inference along the baseline algorithms. We assume the followings for the analysis: 1) The simulation budget per a round is given to  $N$ ; 2) The number of training epoch is shared by  $E$ ; 3) It takes  $B_1$ ,  $B_2$ , and  $B_3$  number of operations to compute the neural posterior in APT, the neural discriminator in AALR, and the neural likelihood in SNL, respectively.

The total complexity of our model is increased by  $O(rNE(2B_1 + B_3))$ , but the increment is minor if the representation powers for APT and SNL,  $B_1$  and  $B_3$ , are at the identical complexity level. Note that this linear-scale discrepancy of complexity would negligible compared to the expensive simulation execution time.

## D. Experimental Details

We release the code at [https://github.com/Kim-Dongjun/Posterior\\_Aided\\_Regularization\\_for\\_Likelihood\\_Free\\_Inference](https://github.com/Kim-Dongjun/Posterior_Aided_Regularization_for_Likelihood_Free_Inference) for the reproducibility and the detailed experimental setup. We make use of the Neural Spline Flow (NSF) (Durkan et al., 2020) for the conditional densities in SNL and APT. We use four spline transforms, where each transformation includes two-blocks of residual networks (He et al., 2016) with the ReLU activation function, and each transformation is partitioned by 64 bins. We use the python package, Simulation-Based Inference (SBI) (Tejero-Cantero et al., 2020), for the calculation of  $\tilde{q}_\phi(\theta|x)$  in APT. We use three-layered fully connected network of 256 neurons for each layers with the ReLU activation function for AALR. We use the Adam optimizer with learning rate of 1E-3,  $(\beta_1, \beta_2) = (0.5, 0.999)$ , and weight decay of 1E-5. On SPNE-A and SNPE-B, we follow the experimental details of the original papers (Papamakarios & Murray, 2016) and (Lueckmann et al., 2018) for the experiments, respectively.

Throughout the inference, we use the early-stopping (Caru-

ana et al., 2001) if no validation loss is improved more than 20 epochs, where 10% of the simulation budget is the validation data. In order to prevent the learning instability, we clip the gradient norm (Pascanu et al., 2013) to five for NSF of SNL and one for NSF of APT. The new simulation inputs are sampled from the Metropolis-Hastings sampler with  $N$ -chains, i.e. we draw batch of next simulation inputs from the independent Markov chains (Kim et al., 2020b). Note that all experiments are replicated 30 times to obtain stable statistics for the experimental results on Intel Core i7/NVIDIA RTX 3090.

As the performance metrics, we use the negative log probability at the groundtruth parameters (Papamakarios & Murray, 2016). The groundtruth parameters include the true parameter ( $\theta_1^*$ ) and the alternative parameters ( $\theta_2^*$ ). The alternative parameter denotes the parameters that generate identical likelihood function, i.e  $p(x|\theta_1^*) = p(x|\theta_2^*)$ . The negative log probability is defined by  $-\log p(\theta^*|x_o) := -\sum_{k=1}^K \log p(\theta_k^*|x_o)$ , where  $\theta_{1:K}^*$  are the groundtruth parameters.

Alternatively, we use the Inception Score (Salimans et al., 2016) to measure the sample quality. The Inception Score calculates the KL divergence between the conditional and the marginal class distributions:  $IS = \exp(\mathbb{E}_\theta[D_{KL}(p(c|\theta) \| p(c))])$ , where the conditional distribution,  $p(c|\theta)$ , is the probability of  $\theta$  being classified by the  $c$ -th cluster. As the conditional distribution, we train the Gaussian Mixture Model with 5,000 samples from the true posterior distribution.

In Figure 4 of the main paper, we follow Mutual Information Neural Estimation (MINE) (Belghazi et al., 2018) to estimate the mutual information of two random variables. We use a three-layered fully connected neural network of 100 neurons, and the ReLU activation function.

## E. Additional Experimental Results

### E.1. Additional Results on Tractable Simulations

Figure 10 and Figure 11 shows the full comparison with respect to every performance metric on both SLCP-16 and SLCP-256 simulations. Figure 10 (a) shows that SNL regularized by PAR obtains a smoother learning curve compared to the unregularized SNL. Figure 10 (b) proves that the true posterior distribution of SLCP-16 is only obtainable with SNL with PAR. If we move on to the SLCP-256 simulation, AALR eventually yields a comparable performance for all metrics. However, the saturation of SNL with PAR is faster than AALR and SNL for every metric.

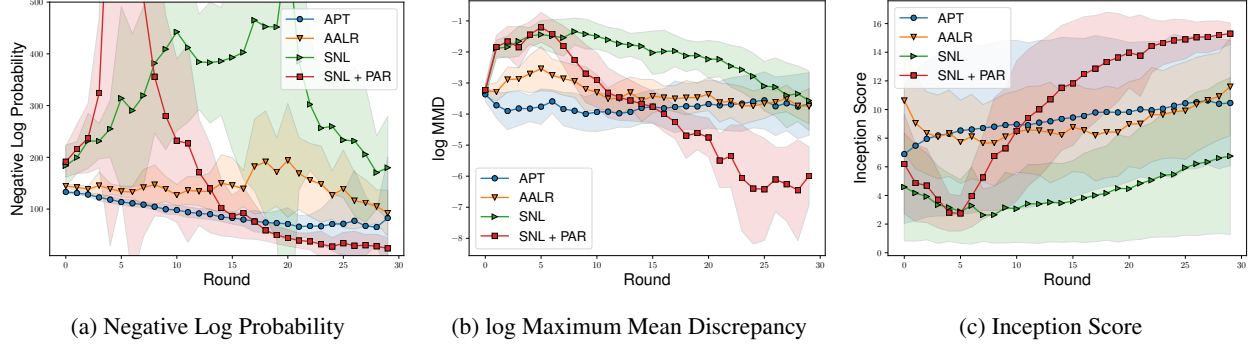


Figure 10. Comparison of all performance metrics by round on SLCP-16 of 50-dimensional output with 100 simulation budget for each round.

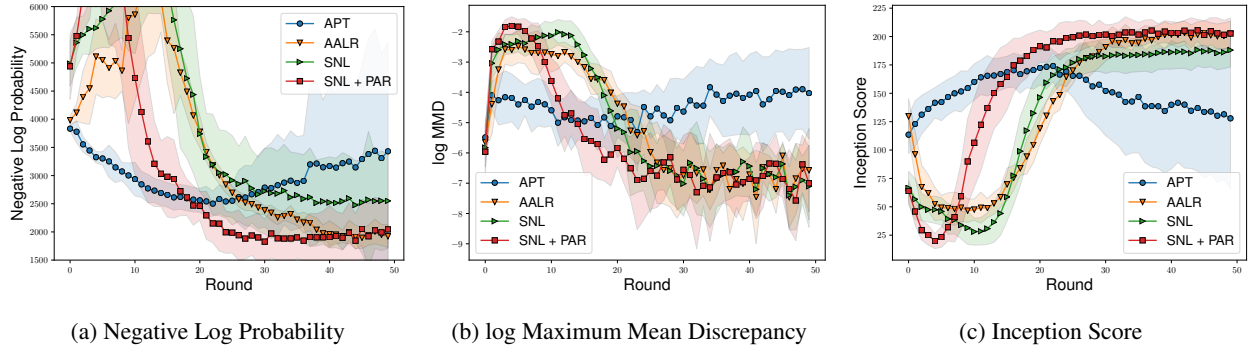


Figure 11. Comparison of all performance metrics by round on SLCP-256 of 40-dimensional output with 100 simulation budget for each round.

## E.2. Comparison of Forward KL/Reverse KL/JJS Divergences

The experimental result in this section indeed motivates us to introduce a regularization technique. Figure 12 presents the marginal posterior after the inference with (a) the forward KL minimization, (b) the reverse KL minimization, and (c) the Jensen-Shannon (JS) divergence minimization on the SLCP-256 simulation of 40-dimensional output. In order to minimize the reverse KL divergence and the JS divergence, we train NSF parameters under the adversarial framework in this experiment. We use the variational divergence minimization (Nowozin et al., 2016), or f-GAN that makes use of the normalizing flow model as a generator. As reported in Grover et al. (2018); Danihelka et al. (2017), the training of a normalizing flow model with the adversarial concept might yield extremely poor log-likelihood scores. Having said that, we suggest Figure 12 to qualitatively investigate the effect of divergences on the inference, rather than the quantitative comparison.

Figure 12 (a) presents the *mode covering* property of the forward KL divergence, and Figure 12 (b) shows the *mode seeking* property of the reverse KL divergence. On the other hand, Figure 12 (c) illustrates the poor performance by cap-

turing a few modes. Figure 12 provides three implications. First, we need to infer the posterior with MLE rather than the adversarial training as long as we insist modeling the neural likelihood by a normalizing flow. Second, the reverse KL divergence would help learning the posterior. Third, we need another regularizing term to avoid the mode collapse if we combine the forward KL and the reverse KL divergences. These three implications motivate us to introduce PAR that 1) still trains the normalizing flow model by MLE, 2) regularizes the original loss (forward KL divergence) with the reverse KL divergence, and 3) regularizes with the mutual information which mitigates the mode collapse by providing the discriminative conditional likelihood given distinctive simulation inputs.

## E.3. Likelihood-Free Inference on Image Generation Models

While VAE targets to estimate the posterior distribution by an auto-encoder structure with the marginal distribution modeling, *likelihood-free inference* infers the posterior distribution with the joint distribution modeling. The posterior estimation of two unsupervised approaches differs by their use-cases; VAE infers the posterior distribution under an ample size of dataset, and *likelihood-free inference* estimates

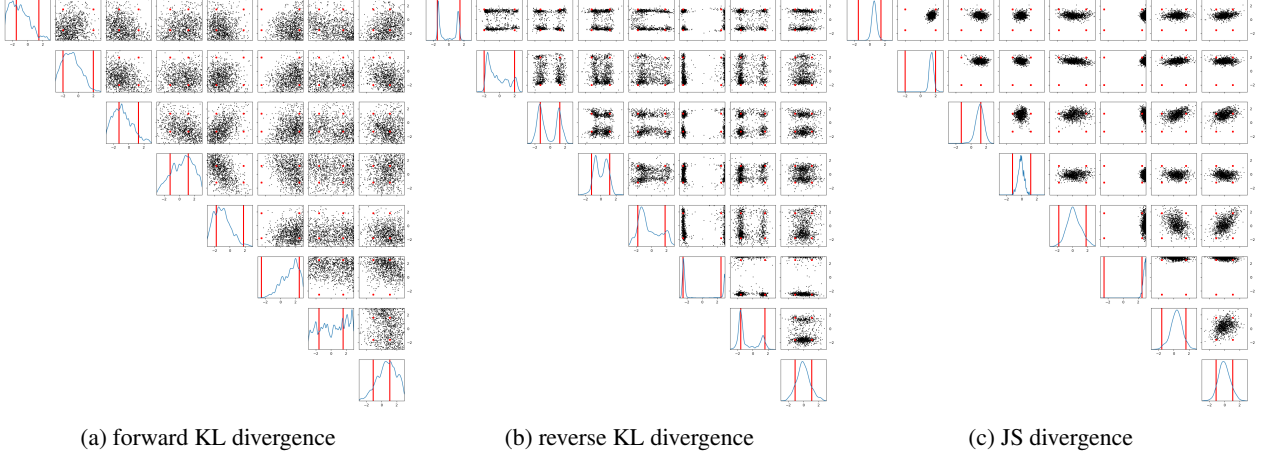


Figure 12. Comparisons of the marginal posterior inferred by forward KL/reverse KL/JS divergences learning with the variational divergence minimization.

the approximate posterior of a fixed simulation model by constructing a cumulative generated dataset.

Although the field of *likelihood-free inference* largely focuses on simulation models, we expand the usability of *likelihood-free inference* on various image generation models. Image data is particularly challenging on *likelihood-free inference* because the multi-class of images induces a highly multi-modal joint distribution. Hence, we qualitatively inspect the regenerated images if the inference algorithm captures the semantic information of the observation, while retaining the generated image quality.

We use a pre-trained Generative Adversarial Network (GAN) generator as a simulation model with the input as a noise and the output as an image, and we extract the summary statistics of a raw image data as the encoded representation of the pre-trained Variational Auto-Encoder (VAE). We use the generative model’s network architecture of Chen et al. (2016), and we train this generative model by the WGAN loss (Arjovsky et al., 2017) with gradient penalty (Gulrajani et al., 2017). The generative model is pre-trained for 100 epochs with the batch size of 64, and with the Adam optimizer of learning rate to be 0.0002. Also, we train the encoder network of three-layered convolutional networks for 50 epochs with 128 batch size by the Adam optimizer of learning rate as 0.001.

In this section, we empirically show that SNL with PAR outperforms the baselines in terms of the mode captivity when the underlying joint distribution is highly multi-modal. Also, SNL with PAR captures the latent semantic information the best by estimating the nearest latent embeddings of  $x_o$  with no label information. This best semantic information captured by SNL with PAR provides the high quality image of the regeneration of  $x_o$ .

#### E.4. MNIST

In MNIST dataset, with five-dimensional input, and 10-dimensional encoded output, Figure 13 (a) presents the consistently outperforming performance of SNL with PAR in terms of the negative log probability with 100 simulation budget for each round. Figure 14 compares the baseline models, in which each image is generated by a simulation input drawn from the inferred posterior. The learning speed of AALR to capture the latent embedding of  $x_o$  is too slow because AALR sometimes generate images of label five after the inference. On the other hand, other algorithms regenerate the observation well. We note that this regenerated images could be used to augment a specific data instance.

Figure 15 shows the inferred posteriors by rounds. APT infers the heavy-tailed posterior distribution, and AALR requires more dataset to infer the accurate posterior despite of the use of shallow network for AALR. On the other hand, SNL and SNL regularized by PAR captures the true parameter. In particular, SNL with PAR outperforms SNL in its inference speed that the regularization reduces the number of required simulation budget.

#### E.5. FashionMNIST

In FashionMNIST experiment, we use the identical generative model’s network architecture and the summary statistics’ network architecture of the MNIST experiment. With the seven-dimensional input, 20-dimensional encoded output, and 100 simulation budget for each round, Figure 13 (b) presents that PAR performs the best at the end of the inference. Moreover, Figure 16 shows that PAR regenerates the original observation the best by retaining the essential information of the observation.

## E.6. SVHN

In SVHN dataset, with nine-dimensional input, 20-dimensional encoded output, and 100 simulation budget for each round, Figure 13 (c) shows the consistent outperformance of SNL with PAR out of baselines. Also, Figure 17 shows that PAR regenerates the original observation, while keeping the semantics of the given observation. Figure 18 illustrates that APT and AALR fail at capturing the latent embedding of  $x_o$  after rounds of inference. Moreover, SNL with PAR captures the latent embedding of  $x_o$  better than the vanilla SNL.

## References

Arjovsky, M., Chintala, S., and Bottou, L. Wasserstein gan. *arXiv preprint arXiv:1701.07875*, 2017.

Bachman, P., Hjelm, R. D., and Buchwalter, W. Learning representations by maximizing mutual information across views. In *Advances in Neural Information Processing Systems*, pp. 15535–15545, 2019.

Belghazi, M. I., Baratin, A., Rajeshwar, S., Ozair, S., Bengio, Y., Courville, A., and Hjelm, D. Mutual information neural estimation. In *International Conference on Machine Learning*, pp. 531–540. PMLR, 2018.

Caruana, R., Lawrence, S., and Giles, L. Overfitting in neural nets: Backpropagation, conjugate gradient, and early stopping. *Advances in neural information processing systems*, pp. 402–408, 2001.

Chen, X., Duan, Y., Houthooft, R., Schulman, J., Sutskever, I., and Abbeel, P. Infogan: Interpretable representation learning by information maximizing generative adversarial nets. *arXiv preprint arXiv:1606.03657*, 2016.

Danihelka, I., Lakshminarayanan, B., Uria, B., Wierstra, D., and Dayan, P. Comparison of maximum likelihood and gan-based training of real nvp. *arXiv preprint arXiv:1705.05263*, 2017.

Durkan, C., Bekasov, A., Murray, I., and Papamakarios, G. nflows: normalizing flows in PyTorch, November 2020. URL <https://doi.org/10.5281/zenodo.4296287>.

Greenberg, D., Nonnenmacher, M., and Macke, J. Automatic posterior transformation for likelihood-free inference. In *International Conference on Machine Learning*, pp. 2404–2414, 2019.

Grover, A., Dhar, M., and Ermon, S. Flow-gan: Combining maximum likelihood and adversarial learning in generative models. In *Proceedings of the AAAI Conference on Artificial Intelligence*, volume 32, 2018.

Gulrajani, I., Ahmed, F., Arjovsky, M., Dumoulin, V., and Courville, A. C. Improved training of wasserstein gans. In *Advances in neural information processing systems*, pp. 5767–5777, 2017.

Gutmann, M. U. and Corander, J. Bayesian optimization for likelihood-free inference of simulator-based statistical models. *The Journal of Machine Learning Research*, 17 (1):4256–4302, 2016.

He, K., Zhang, X., Ren, S., and Sun, J. Deep residual learning for image recognition. In *Proceedings of the IEEE conference on computer vision and pattern recognition*, pp. 770–778, 2016.

Hermans, J., Begy, V., and Louppe, G. Likelihood-free mcmc with amortized approximate ratio estimators. In *International Conference on Machine Learning*, 2020.

Hjelm, R. D., Fedorov, A., Lavoie-Marchildon, S., Grewal, K., Bachman, P., Trischler, A., and Bengio, Y. Learning deep representations by mutual information estimation and maximization. *arXiv preprint arXiv:1808.06670*, 2018.

Ke, L., Barnes, M., Sun, W., Lee, G., Choudhury, S., and Srinivasa, S. Imitation learning as  $f$ -divergence minimization. *arXiv preprint arXiv:1905.12888*, 2019.

Kim, D., Joo, W., Shin, S., and Moon, I.-C. Adversarial likelihood-free inference on black-box generator. *arXiv preprint arXiv:2004.05803*, 2020a.

Kim, D., Song, K., Kim, Y., Shin, Y., and Moon, I.-C. Sequential likelihood-free inference with implicit surrogate proposal. *arXiv preprint arXiv:2010.07604*, 2020b.

Lee, K. S., Tran, N.-T., and Cheung, N.-M. Infomax-gan: Improved adversarial image generation via information maximization and contrastive learning. In *Proceedings of the IEEE/CVF Winter Conference on Applications of Computer Vision*, pp. 3942–3952, 2020.

Lueckmann, J.-M., Goncalves, P. J., Bassetto, G., Oecal, K., Nonnenmacher, M., and Macke, J. H. Flexible statistical inference for mechanistic models of neural dynamics. In *Neural Information Processing Systems (NIPS 2017)*, 2018.

Nguyen, T., Le, T., Vu, H., and Phung, D. Dual discriminator generative adversarial nets. In *Advances in neural information processing systems*, pp. 2670–2680, 2017.

Nowozin, S., Cseke, B., and Tomioka, R. f-gan: Training generative neural samplers using variational divergence minimization. In *Advances in neural information processing systems*, pp. 271–279, 2016.

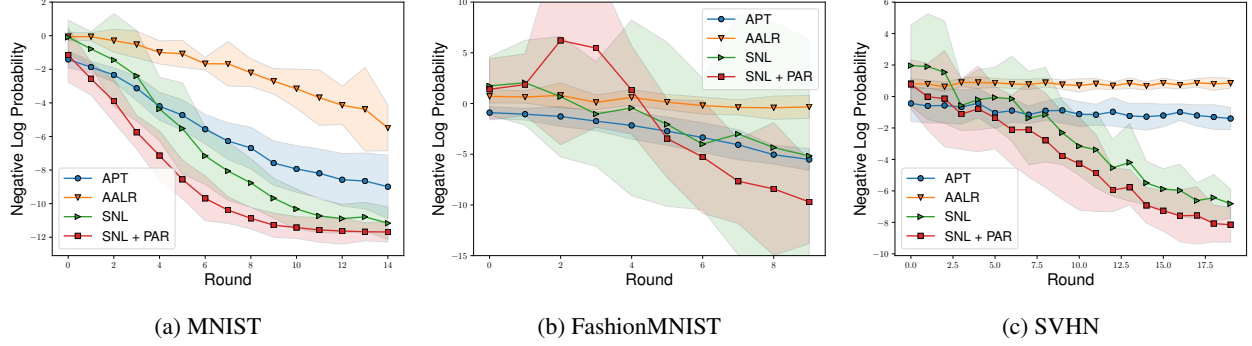


Figure 13. Comparisons of baselines on (a) MNIST, (b) FashionMNIST, and (c) SVHN image generation models.

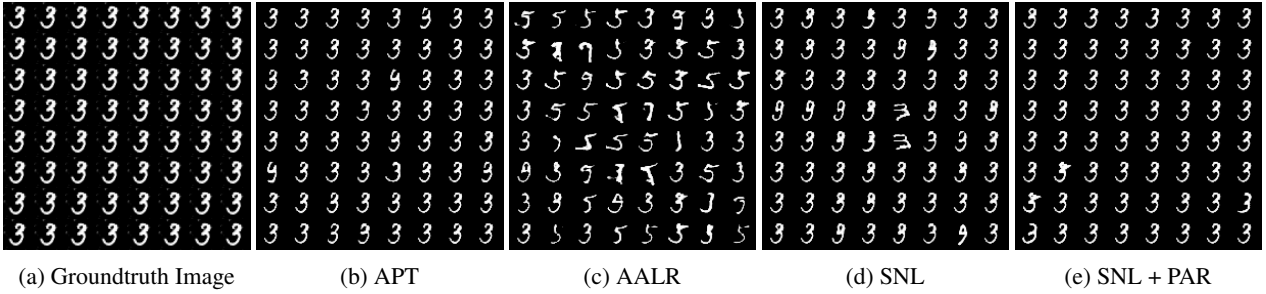


Figure 14. Comparison of the regenerated MNIST images after the inference.

Papamakarios, G. and Murray, I. Fast  $\varepsilon$ -free inference of simulation models with bayesian conditional density estimation. In *Advances in Neural Information Processing Systems*, pp. 1028–1036, 2016.

Papamakarios, G., Sterratt, D., and Murray, I. Sequential neural likelihood: Fast likelihood-free inference with autoregressive flows. In *The 22nd International Conference on Artificial Intelligence and Statistics*, pp. 837–848, 2019.

Pascanu, R., Mikolov, T., and Bengio, Y. On the difficulty of training recurrent neural networks. In *International conference on machine learning*, pp. 1310–1318. PMLR, 2013.

Peng, J., Pedersoli, M., and Desrosiers, C. Mutual information deep regularization for semi-supervised segmentation. In *Medical Imaging with Deep Learning*, pp. 601–613. PMLR, 2020.

Poole, B., Alemi, A. A., Sohl-Dickstein, J., and Angelova, A. Improved generator objectives for gans. *arXiv preprint arXiv:1612.02780*, 2016.

Poole, B., Ozair, S., Van Den Oord, A., Alemi, A., and Tucker, G. On variational bounds of mutual information. In *International Conference on Machine Learning*, pp. 5171–5180. PMLR, 2019.

Salimans, T., Goodfellow, I., Zaremba, W., Cheung, V., Radford, A., and Chen, X. Improved techniques for training gans. In *Advances in neural information processing systems*, pp. 2234–2242, 2016.

Shao, J., Wang, Q., and Liu, F. Learning to sample: an active learning framework. In *2019 IEEE International Conference on Data Mining (ICDM)*, pp. 538–547. IEEE, 2019.

Sisson, S. A., Fan, Y., and Tanaka, M. M. Sequential monte carlo without likelihoods. *Proceedings of the National Academy of Sciences*, 104(6):1760–1765, 2007.

Sriperumbudur, B. K., Gretton, A., Fukumizu, K., Schölkopf, B., and Lanckriet, G. R. Hilbert space embeddings and metrics on probability measures. *The Journal of Machine Learning Research*, 11:1517–1561, 2010.

Tejero-Cantero, A., Boelts, J., Deistler, M., Lueckmann, J.-M., Durkan, C., Gonçalves, P. J., Greenberg, D. S., and Macke, J. H. sbi: A toolkit for simulation-based inference. *Journal of Open Source Software*, 5(52):2505, 2020. doi: 10.21105/joss.02505. URL <https://doi.org/10.21105/joss.02505>.

Wood, S. N. Statistical inference for noisy nonlinear ecological dynamic systems. *Nature*, 466(7310):1102–1104, 2010.

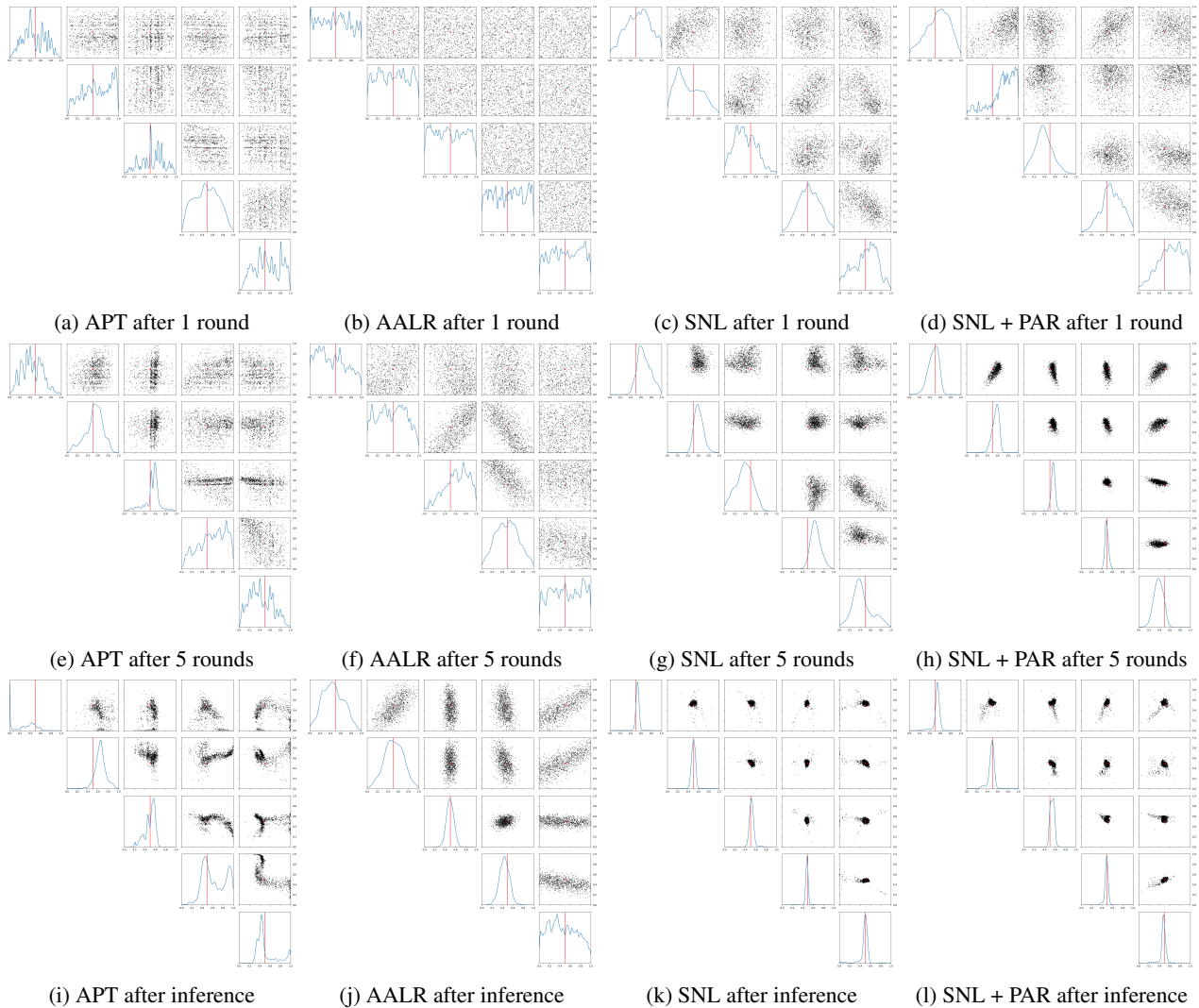
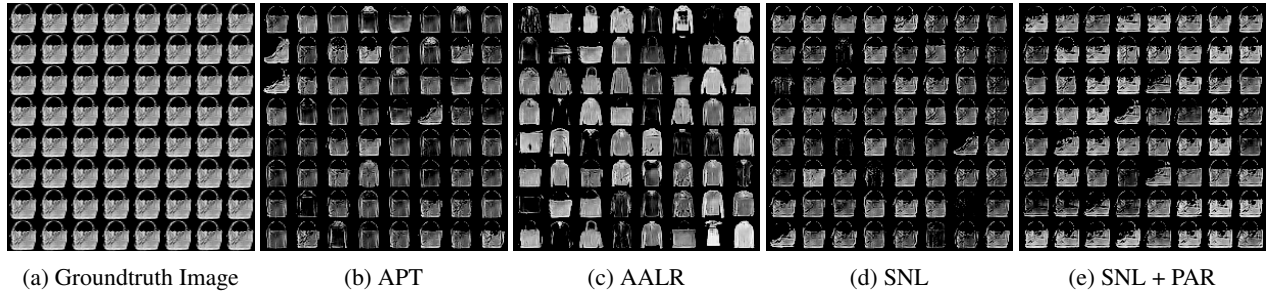


Figure 15. Comparison of the marginal posterior distributions on the MNIST dataset by rounds.

Zhang, M., Bird, T., Habib, R., Xu, T., and Barber, D. Variational f-divergence minimization. *arXiv preprint arXiv:1907.11891*, 2019.

Zhao, S., Song, J., and Ermon, S. Infovae: Information maximizing variational autoencoders. *arXiv preprint arXiv:1706.02262*, 2017.



(a) Groundtruth Image      (b) APT      (c) AALR      (d) SNL      (e) SNL + PAR

Figure 16. Comparison of the regenerated Fashion MNIST images after the inference.



(a) Groundtruth Image      (b) APT      (c) AALR      (d) SNL      (e) SNL + PAR

Figure 17. Comparison of the regenerated SVHN images after the inference.

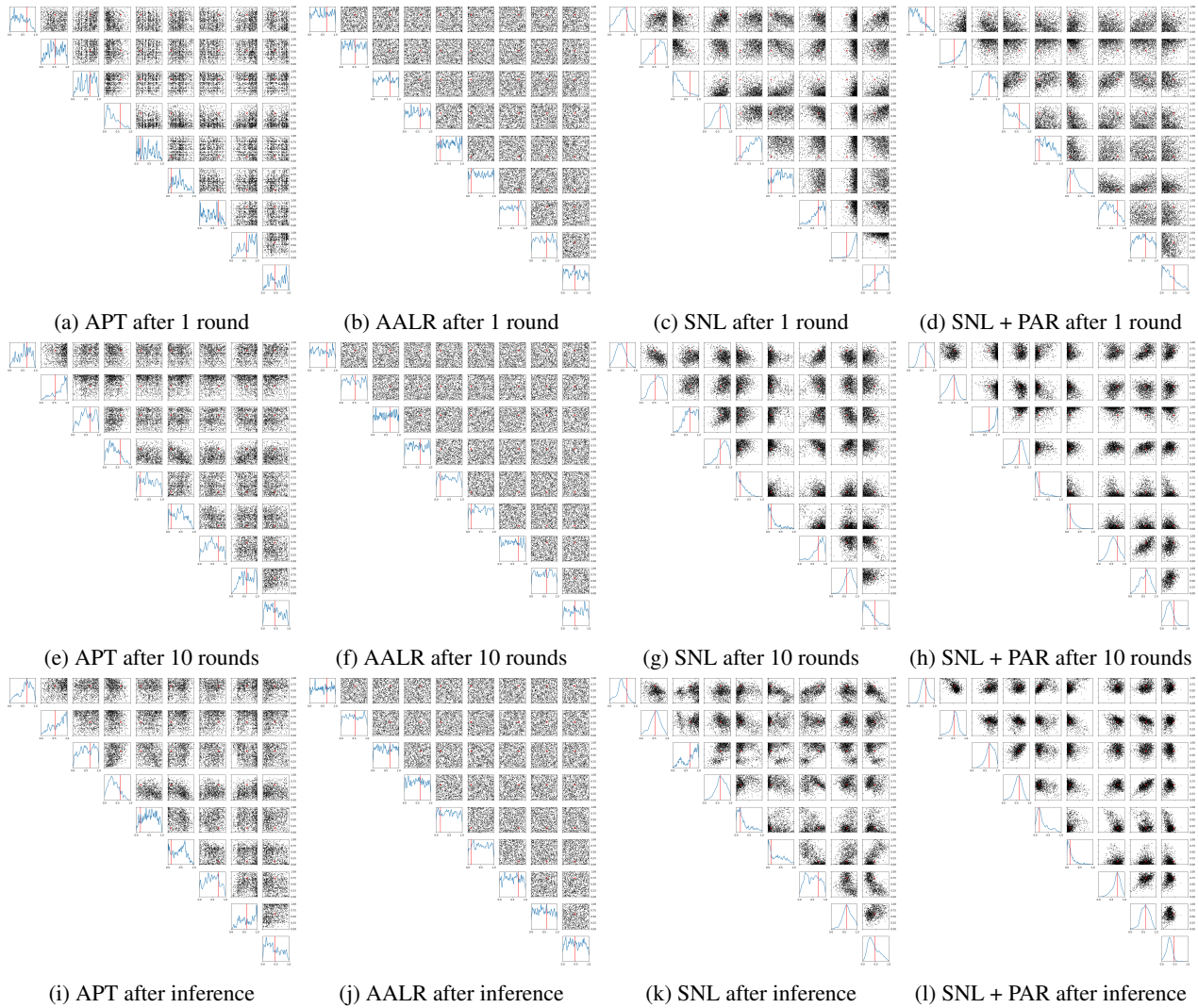


Figure 18. Comparison of the marginal posterior distributions on the SVHN dataset by rounds.